Deep-Tropospheric Gravity Waves Created by Leeside Cold Fronts

F. M. RALPH AND P. J. NEIMAN

Environmental Technology Laboratory, NOAA/ERL, Boulder, Colorado

T. L. KELLER

Research Applications Program, NCAR, Boulder, Colorado

(Manuscript received 7 October 1998, in final form 20 November 1998)

ABSTRACT

The water vapor channel of the Geostationary Operational Environmental Satellite *GOES-8* reveals narrow (30 km wide), elongated (500–1000 km) bands that propagate southward on the eastern side of the Rocky Mountains from Colorado to Texas. Two events in which surface and wind profiler observations show that these bands are associated with leeside cold fronts are documented in detail, and several other cases are summarized. The wind profilers observe vertical motions exceeding 1 m s^{-1} in narrow plumes at the leading edge of the fronts, in broader zones in the upper troposphere, and in the lower stratosphere. These cause vertical displacements of up to 1 km and are responsible for the signature in water vapor images.

The bands occur when the Rocky Mountains block either arctic leeside cold fronts coming from the north or northeast or Pacific cold fronts coming from the northwest. The blocking changes the frontal orientation and disrupts geostrophic thermal wind balance near the terrain-modified fronts. This imbalance is manifested as strong (20 m s^{-1}) prefrontal, front-relative, cross-front flow V_r. Observations and numerical simulations are presented showing that deep-tropospheric gravity waves are produced in this region by the obstacle effect of the surface leeside cold front. Farther east, V_r is near zero, and the waves are weak or absent.

Along the western portion of the front the waves propagate with the front and resemble trapped lee waves; however, farther east the waves appear ahead of the surface front by up to 100 km. These prefrontal gravity waves occur when the wave forcing decays along the eastern portion of the front and the trapped waves that had developed there become decoupled from the front and propagate away. Numerical simulations of a well-observed event confirm that trapped waves would have developed, and profiler data confirm the trapped nature of the observed gravity wave's vertical structure. Such waves could create convection, including prefrontal squall lines, and can be seen in real-time satellite imagery before the convection is triggered.

1. Introduction

Theoretical and numerical studies have indicated that gravity waves can be produced in response to frontogenesis (Ley and Peltier 1978; Gall et al. 1988; Garner 1989; Snyder et al. 1993), although little observational documentation of this behavior has been presented. However, it has been shown that as the spatial scale of a cold front contracts, the front can take on key characteristics of gravity currents, including their sharp density contrast and headlike structure (Carbone 1982; Hobbs and Persson 1982; Shapiro 1984; Young and Johnson 1984; Seitter and Muench 1985; Shapiro et al. 1985; Miller et al. 1996). Under these conditions observations have clearly revealed the generation of gravity waves by fronts. Gravity wave generation associated with gravity currents can occur through the creation of internal bores, which can propagate out ahead of a front (e.g., Tepper 1950; Simpson 1987; Crook 1988; Haase and Smith 1989; Doviak et al. 1991; Klemp et al. 1997), Kelvin–Helmholtz instability on the cold-air interface (Mueller and Carbone 1987; Droegemeier and Wilhelmson 1987; Parsons et al. 1991; Weckwerth and Wakimoto 1992; Ralph et al. 1993b; Jin et al. 1996), or through the effect of the front as an obstacle (Ralph et al. 1993b; Jin et al. 1996). Because the studies cited focused on lower-tropospheric measurements, little is known of deep-tropospheric gravity waves produced by fronts except that wind profiling radars and commercial aircraft have observed enhanced vertical velocity variance at high altitudes in the vicinity of surface cold fronts (Nastrom et al. 1990; Fritts and Nastrom 1992). An alternative hypothesis that the observed bands are a manifestation of purely frontal circulations associated with the shallow cold fronts is not explored because it is inconsistent with the presence of multiple narrow bands and the fact that strong perturbations are found

Corresponding author address: Dr. F. Martin Ralph, NOAA/ERL/ETL, Mail code R/E/ET7, 325 Broadway, Boulder, CO 80303.
E-mail: fralph@etl.noaa.gov

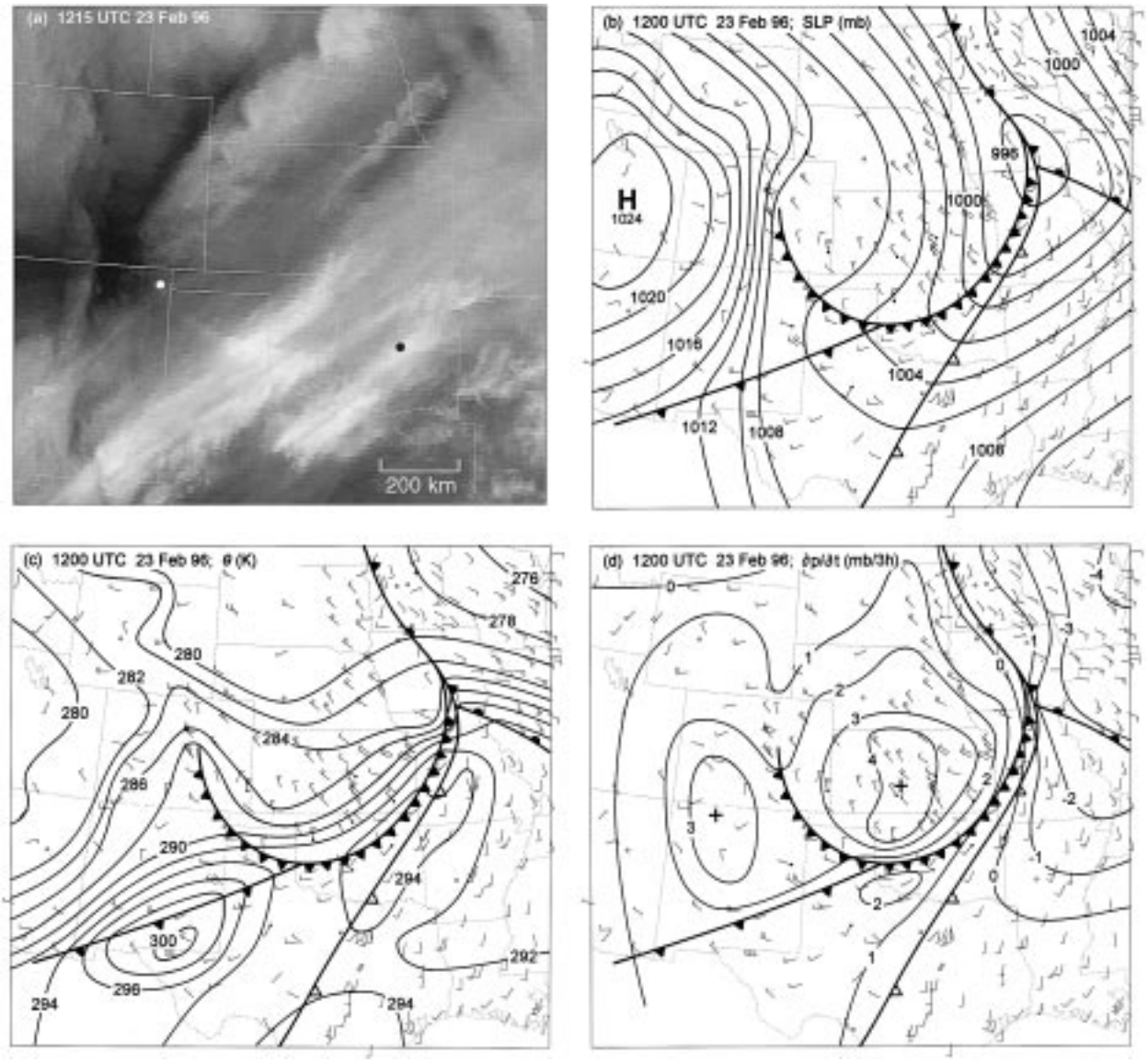

FIG. 1. (a) *GOES-8* water vapor channel (6.7 μm) satellite image of a leeside frontal gravity wave on 23 February 1996. The west and east ends of the wave perturbation are highlighted by the large white and black dots, respectively. Note that the wave extends across the southwest-northeast-oriented moist bands and cirrus clouds. Surface analyses are of (b) mean sea level pressure (mb), (c) surface potential temperature (K), and (d) 3-h surface pressure change (mb). Surface wind flags = 25 m s^{-1}, barbs = 5 m s^{-1}, and half barbs = 2.5 m s^{-1}. Wind profiler sites with surface data are marked by small dots in (b), (c), and (d). The leeside cold front is distinguished graphically from the rest of the Pacific cold front by using cold-frontal symbols that are closely spaced.

in the upper troposphere, well above the shallow frontal updraft. The well-documented connection between the bands and surface cold fronts described in this paper indicates that geostrophic adjustment or vertical shear instability, which can create gravity waves in similar environments with strong upper-tropospheric jet–front systems (e.g., Stobie et al. 1983; Uccellini and Koch 1987; Bosart and Seiman 1988; Koch et al. 1993), are not the source. Also, the absence of deep convection rules out thunderstorms as the source of the disturbances (e.g., Curry and Murty 1974). The goals of this paper are to present unique evidence of deep-tropospheric gravity waves associated with surface cold fronts, including waves up to 100 km ahead of the front, and to describe their synoptic environment, their relationship to fronts, and their origins. The fronts and waves described in this paper exist just east of the Rocky Mountains where the western Great Plains have a roughly 1/500 slope.

We first saw the waves in images (Figs. 1a, 4a, 6, 7a, and 15) from the water vapor channel (6.7 μm) of the *Geostationary Operational Environmental Satellite-8* (*GOES-8*). They are narrow (10–30 km), long (500–1000 km), and propagate southward along the eastern

slope of the Rocky Mountains. Their connection to surface cold fronts became apparent through wind profiler and surface data. The absence of significant cloudiness makes them detectable primarily in water vapor images and suggests that they occur with fronts referred to as ''Blue Northers'' because of the clear skies (Mogil 1985).

Two events are presented to illustrate the range of synoptic conditions under which these waves occur, that is, propagation of a polar cold front from the Pacific Northwest into the Great Plains, which is a situation that has been studied by Mecikalski and Tilley (1992), Bluestein (1993), and Neiman et al. (1994, 1995); and the southward surge of arctic air down the eastern side of the Rocky Mountains, such as has been described by Neiman et al. (1991, 1998), Mecikalski and Tilley (1992), Wang et al. (1995), Colle and Mass (1995), Miller et al. (1996), and Schultz et al. (1997). Both events include disturbances in water vapor imagery that coincide with a surface cold front observed by wind profilers. Evidence is also presented showing waves well ahead of the fronts, and a mechanism linking the prefrontal waves to the front is proposed.

There appears to be a preference for the waves to be produced primarily along the portion of a front that has been modified at the surface by the Rocky Mountains. Recent results from Mecikalski and Tilley (1992) and Colle and Mass (1995) indicate that the terrain-enhanced northerly ageostrophic postfrontal flow often extends 500 km east of the mountains, partly due to the influence of the approximately 1/500 slope of the Great Plains (Colle and Mass 1995). This distance closely matches the domain of the waves documented here.

Relevant capabilities and limitations of the key observing systems are described in section 2. Section 3 documents the synoptic-scale conditions of the two events and lists several additional cases. Section 4 presents the detailed measurements of the waves and the fronts in each of the two cases, including intriguing differences between the finescale structures of the surface fronts. The origins of the waves are explored with the aid of a two-dimensional, nonlinear, nonhydrostatic numerical model in section 5. The results are then summarized, and their implications for the generation of prefrontal deep convection are discussed in section 6.

2. Overview of key observing systems

The radar wind profilers used here are from the National Oceanic and Atmospheric Administration (NOAA) Profiler Network (Barth et al. 1994; Ralph et al. 1995). They measure wind in clear, cloudy, and precipitating conditions at 0.25-km vertical intervals from 0.5 to 16.5 km above ground level (AGL) using three beam orientations: one vertical and two at 16.5° from zenith pointing roughly east and north. Hourly averaged and 6-min–time resolution horizontal winds are used. The assumptions and limitations of each type of measurement, and the use of spectral moment data, are described in Ralph et al. (1995). Wind profilers have been useful in documenting fronts (e.g., Neiman and Shapiro 1989; Crochet et al. 1990; Neiman et al. 1991, 1992, 1998; Ralph et al. 1993b) and gravity waves (e.g., Ecklund et al. 1982; Lu et al. 1984; Sato 1990; Ralph et al. 1992, 1993a,b, 1997; Prichard et al. 1995; Trexler 1997). As with earlier gravity wave studies, the vertical air motion measurements are used to document such waves in the troposphere and lower stratosphere. Results from studies summarized in Ralph et al. (1997) suggest that the accuracy of profiler vertical motion measurements can be on the order of ± 0.1 m s^{-1}. Surface measurements from many of the profiler sites are also used here, as are standard hourly surface airway observations.

The *GOES-8* water vapor channel measures 6.7-μm-wavelength radiance upwelling from the atmosphere that originates from a layer that is usually between 700 and 300 mb (Weldon and Holmes 1991). Because the radiance depends on the moisture content and air temperature, areas of high-altitude moisture appear cold (bright), and areas where upper-levels are dry appear warm (dark). Interleaving moist layers, and clouds can degrade this interpretation. These data have helped identify mesoscale features in the upper troposphere in upper fronts and cyclones (e.g., Muller and Fuelberg 1990; Appenzeller and Davies 1992; Ralph 1996; Appenzeller et al. 1996). The image navigation is accurate to within one pixel, which is 8 km wide. The brightness and contrast of each complete original image were adjusted digitally to show the waves. The most effective way to view the evolution of these waves is in continuous temporal loops. Unfortunately, here it is only possible to present individual frames.

3. Synoptic-scale environments

a. Cases identified by the presence of perturbations in water vapor images

The first time that we noticed the long, narrow, southward-propagating perturbations in water vapor–channel satellite images was on 19 October 1995. This was soon after the *GOES-8* imagery, which has 8-km spatial resolution compared with 14 km on *GOES-7*, became regularly available on the DARE [Denver AWIPS (Automated Weather Information Processing System) Risk Reduction and Requirements Evaluation] workstation developed at NOAA's Forecast Systems Laboratory. (Henceforth we will refer to these perturbations as gravity waves on the basis of analyses presented later.) These waves were also noticed by the Science and Operations Officer at the Denver National Weather Service Forecast Office where the DARE workstation was being tested for operational use (Eric Thaler 1995, personal communication). Over the next 18 months seven more events with similar water vapor signatures were ob-

TABLE 1. Overview of eight leeside frontal gravity wave events observed east of the Rocky Mountains over Colorado, Kansas, Oklahoma, New Mexico, and Texas. Times that the perturbation was visible in water vapor images and maximum 3-h postfrontal surface pressure rises ΔP are given. Temperature data at 850 mb from the standard 12-hourly rawinsondes are as follows: maximum local 12-h temperature change, $\partial T/\partial t$ (three-letter station identifiers: LBF, North Platte, Nebraska; AMA, Amarillo, Texas; DDC, Dodge City, Kansas; RAP, Rapid City, South Dakota); maximum temperature decrease over 360 km north–south, and minimum temperature within roughly 1000 km north of the leeside front, T_{min}, from operational isotherm analyses.

		850-mb temperature data			
Date	Time visible (UTC)	$\partial T/\partial t$ (°C/12 h)	$\partial T/\partial y$ (°C/360 km)	T_{min} (°C)	ΔP (mb)
19 Oct 1995	0900–1800	−14 (LBF)	−18	−1	8.0
11 Jan 1996	0000–0400	−13 (AMA)	−12	−2	6.4
10 Feb 1996	1200–1900	−19 (LBF)	−20	−11	5.6
23 Feb 1996*	0700–1500	−17 (DDC)	−15	−2	6.1
6 Mar 1996	1000–1800	−23 (AMA)	−25	−25	6.4
16 Mar 1996	0800–1700	−13 (RAP)	−9	−7	6.0
27 Jan 1997*	1700–2100	−19 (AMA)	−25	−25	8.0
8 Apr 1997	1800–0000	−15 (AMA)	−21	−10	6.1
Average		−17	−18		6.6

* Events described in detail in this paper.

served and archived (Table 1). Although the region examined in the satellite imagery covered most of the western United States, no southward-propagating leeside waves were seen in the water vapor imagery north of central Wyoming or south of the Texas–Mexico border. Because the real-time data were examined on only about 30% of the days during that period, and because not all events were entered into the archive, it is estimated that this total is less than one-fourth of all observable similar events in that period.

It became evident that the waves in the satellite images occurred in connection with leeside cold fronts (e.g., Figs. 1b–d) and often occurred in the absence of precipitation or cloud. The temperature changes with the fronts are given in Table 1, which uses hourly surface data and 12-hourly rawinsonde data from the operational observing network from Montana to Texas. The times in Table 1 are roughly centered on the period that waves were observed by satellite. The maximum 12-h decrease in 850-mb temperatures observed by rawinsonde in each case at sites east of the Rocky Mountains ranges from 13° to 23°C and averages 17°C. Similarly, the maximum north–south temperature gradient at 850 mb is given using a distance scale of 360 km, which is roughly the spacing of the operational synoptic rawinsonde sites from Montana to Texas. This gradient ranges from 9°C/360 km to 25°C/360 km, and averages 18°C/360 km. Much of these temperature changes are probably distributed over shorter distances and times than are measurable with the rawinsondes, as indicated in a case on 27 January 1997 where a radio acoustic sounding system (RASS) at Vici, Oklahoma (not shown), measured a 4-h temperature drop of 23°C, compared to a 19°C drop in 12 h at the Amarillo rawinsonde site.

Table 1 shows that the waves can occur at any time of day from October through April, and have 5.6–8-mb maximum surface pressure rises over 3 h. Some are related to very cold arctic intrusions, such as those where the minimum 850-mb temperature drops below about −10°C over the north-central United States. Such 850-mb temperatures rarely occur with Pacific weather systems, which have usually been warmed by surface sensible heat fluxes from the ocean, latent heating due to precipitation over the mountains, and adiabatic descent from the elevated terrain. This distinction between arctic and Pacific cases is consistent with the classification of 92 cold surges along the Rocky Mountain front range by Mecikalski and Tilley (1992). Schultz et al. (1998) noted that Central American cold surges originating from North Pacific anticyclones that crossed the intermountain western United States had weaker temperature drops (ΔT = 4°–5°C) than those originating from Canadian anticyclones east of the Rockies ($\Delta T \geq$ 9°C). The two events presented in sections 3 and 4 range from a weak Pacific cold front to a strong arctic front. Although this paper does not explore the frequency of occurrence of gravity waves associated with leeside cold fronts, it appears that they are common.

b. Synoptic conditions of 23 February 1996: A Pacific cold front

This event developed when a lower-tropospheric front moved east-southeastward across the Rocky Mountains. This is seen at 850 mb (Fig. 2), where a synoptic-scale trough in the geopotential height field had just crossed the Rockies at 0000 UTC 23 February (Fig. 2a) and the associated cold front extended southwestward from Denver, Colorado, through southwestern New Mexico. This cold front is referred to here as the Pacific front because it is associated with a weather system that had earlier been located over the eastern North Pacific Ocean. The location of the surface anticyclone center over Utah, well west of the Continental Divide, also attests to the Pacific origin of the system (Fig. 1b), especially when compared with the conditions during a true arctic surge described in section 3c (Fig. 4b).

As the Pacific cold front approached Colorado from the west-northwest, its northern section proceeded through the gap in the high terrain in southern Wyoming, while its progress over Colorado was impeded due to blocking by the much taller Colorado Rocky Mountains. Once the northern portion reached eastern Wyoming, it turned southward along the eastern slope of the Colorado Rockies, creating a terrain-induced leeside cold front, such as those studied by Neiman et al. (1994, 1995). The leeside cold front moved southward more slowly close to the mountains than it did farther east over the Plains. This created the characteristic arc-shaped front consisting of a north–south-oriented west-

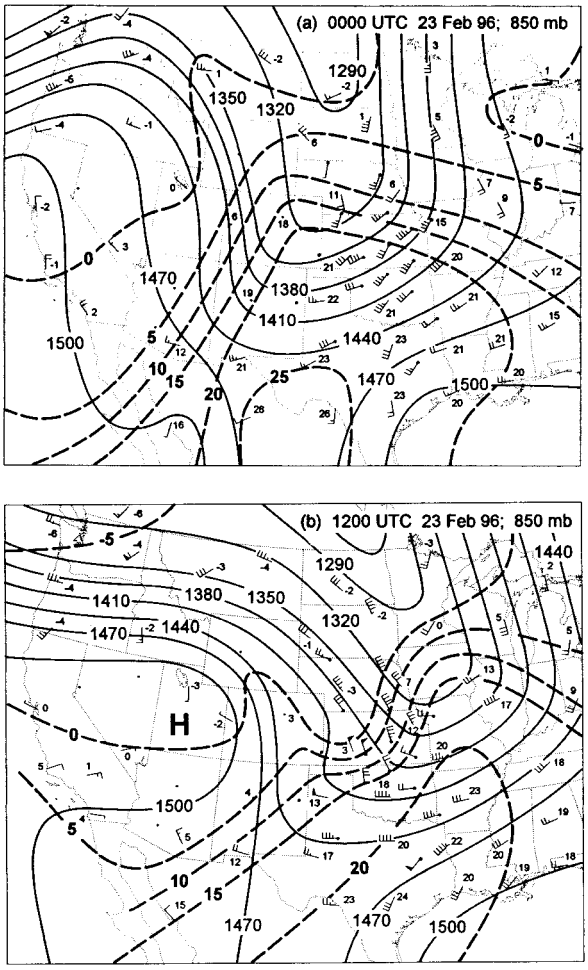

FIG. 2. Geopotential height (m, solid), isotherms (°C, dashed), and winds (as in Fig. 1) at 850 mb on 23 February 1996: (a) 0000 UTC and (b) 1200 UTC. Wind data from profilers are marked with a solid dot; dots are also shown for the Granada, Colorado, and Tucumcari, New Mexico, profiler sites even though the lowest range gate at each site is above 850 mb.

ern portion paralleling the mountains and a southwest-northeast-orientated portion over the Plains (Fig. 1), as seen in other studies (Mecikalski and Tilley 1992; Bluestein 1993; Colle and Mass 1995; Hutchinson and Bluestein 1998).

By 1200 UTC 23 February the trough and cold front at the surface and 850 mb extended from near Des Moines, Iowa, through El Paso, Texas (Figs. 1 and 2). By this time the front had developed a southward bulge and a sharp wind direction shift from southwesterly to north-northwesterly in Kansas, Oklahoma, and Texas (Figs. 1 and 2) that is characteristic of leeside surges (e.g., Mecikalski and Tilley 1992; Bluestein 1993; Colle and Mass 1995). The Pacific front extended southwest of this bulge, from near Amarillo, Texas, to southwestern New Mexico. This part of the front was marked by a less pronounced wind direction shift, pressure trough, and postfrontal pressure rise than in the surge region, but with a comparable potential temperature gradient (Figs. 1b–d). Also, a weak cold front aloft stretched across eastern Oklahoma and central Texas, as indicated by a shift from south-southwesterly to westerly or northwesterly winds and a drop of 3°–6°C at 850 mb between 0000 and 1200 UTC at Midland, Del Rio, and Fort Worth, Texas (Fig. 2); and by a pressure trough without a thermal contrast at the surface (Fig. 1).

At 1200 UTC, the southward-propagating leeside cold front intersected the Pacific front near the border between Oklahoma and the Texas Panhandle (Figs. 1 and 2). (The dynamics that created this frontal orientation remains unclear but probably involved temporal and north–south variations of blocking as the synoptic-scale baroclinic wave crossed the Rocky Mountains.) Because of the difference in potential density the leeside front remained distinct from the Pacific front even where it lagged the Pacific frontal passage. This is illustrated northwest of their juncture by a 3°–4°C temperature contrast, a shift from northwesterly to northerly flow, and the presence of two distinct pressure rise centers separated by the leeside front (Fig. 1). This distinction between the Pacific front and the leeside front is even more apparent in 6-min–time resolution wind profiler and surface measurements at Jayton, Texas, where both fronts passed and were readily distinguishable from one another (Fig. 3). [The location of Jayton, Texas (JTN), is shown in Figs. 4a and 9 and can be seen in Figs. 1–4 as the only profiler site in western Texas.] The Pacific front passed at 1403 ± 3 min UTC, based on a 90° wind direction shift, a 1.2°C temperature drop at a time of diurnal temperature rise, and a 1.1-mb pressure rise in 6 min. Over the next 3 h the pressure rose another 4.5 mb, and the wind direction remained nearly constant at about 330°. These changes at the surface coincided with a wind shift from 25 m s^{-1} westerly to 20 m s^{-1} northwesterly through 2.5 km MSL. The leeside front reached Jayton at 1833 ± 3 min UTC, and was marked by a wind shift from 330° to 030° at the surface and up to 2.0 km mean sea level (MSL). The temperature dropped by 3°C, and the pressure rose by 0.5 mb over the next 0.75 h. Extrapolation of the leeside frontal position based on an isochrone analysis (presented later in Fig. 9) of the waves in water vapor images over 8 h, which in this region coincided with the leading edge of the leeside front, indicated that the front should have passed Jayton at 1825 UTC. This extrapolated time of frontal passage is within 10 min of the observed time of passage. Both fronts were also observed at the Tucumcari, New Mexico, profiler site (not shown).

c. Synoptic conditions of 27 January 1997: An arctic leeside cold front

A second event with waves in water vapor imagery (Fig. 4a) illustrates the behavior in a case characterized by the southward advance of an arctic air mass from central Canada. This type of leeside cold front represents

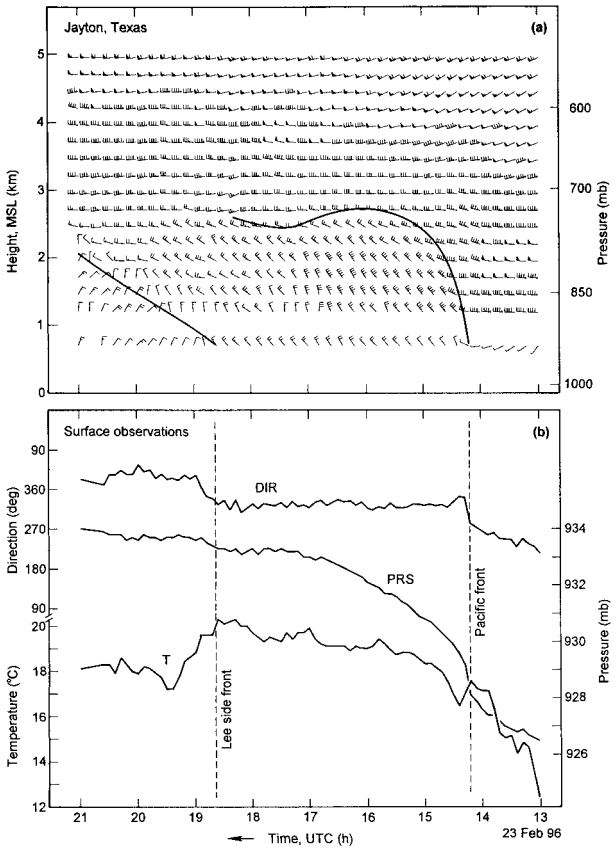

FIG. 3. (a) The 6-min-resolution horizontal winds measured by the 404-MHz radar wind profiler at Jayton, Texas. Its location is shown in Figs. 4a and 9, and can be seen in Figs. 1–4 as the only profiler site in western Texas. Winds are as in Fig. 1. Every other time is omitted for clarity, and one pass of a temporal Hann filter was applied, and edited or missing data points were replaced by interpolation. Collocated surface wind measurements are also shown. (b) Time series of surface wind direction (DIR), pressure (PRS), and temperature (*T*). The upward extension of the Pacific cold front and the leeside cold front are marked in (a), as are the times of their passage at the surface in (b).

87% of the 92 cases studied by Mecikalski and Tilley (1992). The 23 February 1996 and 27 January 1997 fronts had similar maximum 12-h temperature drops at 850 mb (17° and 19°C). However, the minimum 850-mb temperatures (−2° and −25°C) were markedly different, as were the north–south 850-mb temperature gradients (15°C/360 km and 25°C/360 km) (Table 1). The arctic origin of the air mass in this case is illustrated not only by the cold 850-mb temperatures (Fig. 5) but also by the position of the anticyclone center east of the Rockies (Fig. 4b) and by the relative lack of 850-mb temperature gradients or pressure rises west of the central and southern Rocky Mountains (Figs. 4 and 5). This case also contains larger baroclinicity at the surface (Fig. 4c) and a sharper isallobaric gradient (Fig. 4d) than did the 23 February 1996 case (Figs. 1c,d). (The contour interval is 2°C in Fig. 1c and 4°C in Fig. 4c.)

4. Observations of leeside frontal gravity waves and their associated surface cold fronts

a. The 23 February 1996 case

1) SATELLITE OBSERVATIONS OF GRAVITY WAVES

The southward propagation and evolution of the waves on 23 February 1996 is shown using water vapor satellite images (Figs. 6–9) and a single visible image (Figs. 7b and 8b). This and other visible images, along with infrared satellite images (not shown), establish that few clouds were present in the area, other than some jet stream cirrus and a small cloud band 300 km north of the leeside cold front. Thus, it is unlikely that diabatic effects associated with precipitation contributed to wave generation. The following discussion focuses on the single most prominent wave, which is the one seen clearly in the satellite images. Figure 6 shows the propagation of this wave from southern Kansas at 0702 UTC to southern Oklahoma and the Texas Panhandle at 1402 UTC, and a noticeable temporal change in its visual character over 7 h. The wave appears initially as an arc marked by a relatively bright region, with a sharp contrast between it and a broad dark area to its north. This is highlighted over the Oklahoma panhandle in Fig. 7a at 0945 UTC using a trace of the brightness across the wave (Fig. 8a). This shows a south-to-north increase from 150 to 160 counts followed by a decrease to 130 counts, a 20%–25% change. The wave also modulated the albedo of a cirrus cloud (Figs. 7b and 8b).

Isochrones of wave position show the wave propagation between 0702 and 1515 UTC on 23 February (Fig. 9). Satellite data before 0702 UTC were missing, but the image at 0702 UTC suggests the wave should have been visible before then. The wave was last visible at 1515 UTC. The isochrones mark the relatively sharp boundary between the leading brightened region and the dark region to its north. The southward phase speed of the wave varied from 11.9 m s^{-1} along 102°W (Colorado's eastern border) to 19.8 m s^{-1} along 97.5°W (near the Purcell, Oklahoma, profiler site; PRC). Most other features in the water vapor imagery moved northeastward in the upper-level flow, and the wave was clearly propagating against this motion. The wave extended as far east as western Arkansas from 1300 to 1400 UTC but became much less distinct by 1515 UTC. The imperfect, but intriguing, correlation between the position of the leeside cold front at the surface and the wave is also seen in Fig. 9 and is the focus of the following subsection.

Although it would be useful to know precisely what altitude range the water vapor channel is observing in this event, it is very difficult to determine this without performing a complex calculation of the transmittance using a radiative transfer model. However, it is possible to gain some insight through use of an idealized calculation shown in Weldon and Holmes (1991) that uses conditions remarkably similar to two timely moisture

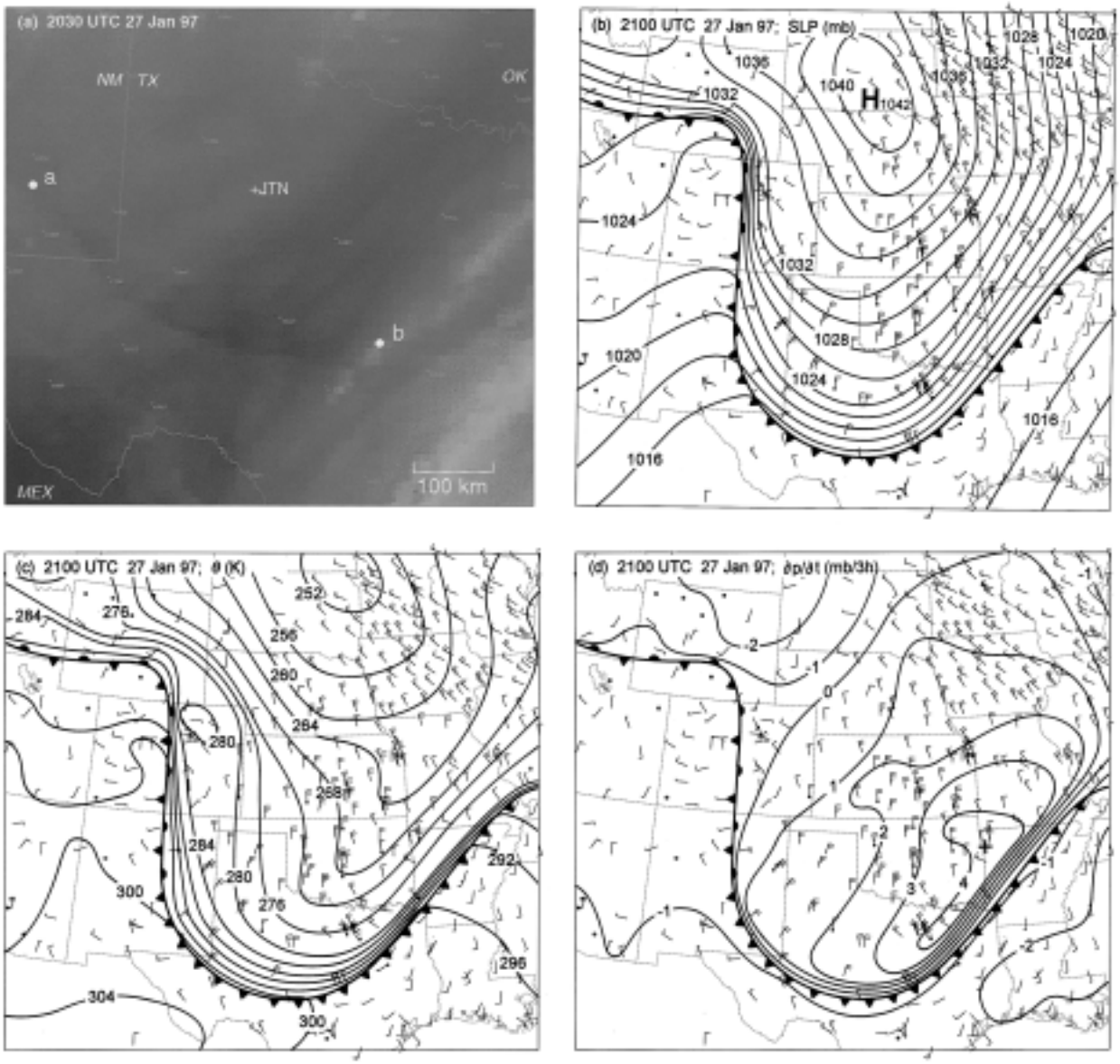

FIG. 4. (a) *GOES-8* water vapor channel (6.7 μm) satellite image of a leeside frontal gravity wave on 27 January 1997. The approximately west and east ends of the wave perturbation are highlighted by the two large dots labeled ''a'' and ''b.'' Note that the wave extends across the southwest-northeast-oriented moist bands. The Jayton, Texas, profiler site is shown (JTN). Surface analyses are of (b) mean sea level pressure (mb), (c) surface potential temperature (K), and (d) 3-h surface pressure change (mb). Fronts, winds, and profiler sites are as in Fig. 1.

profiles available for this case. From the satellite image at 1200 UTC 23 February (Fig. 1a) and the isochrone analysis (Fig. 9), it is apparent that the wave was within 100 km north of soundings launched at that time from Amarillo, Texas, and from Norman, Oklahoma (near PRC in Fig. 9). (The Amarillo sounding is shown later in Fig. 21). Both soundings generally showed a single moist layer (dewpoint depressions of <10°C) between 510 and 400 mb, with much drier conditions above and below that layer. Weldon and Holmes (1991) contains an example (Fig. 15b) for which a single moist layer between 600 and 400 mb was introduced containing 2.1 mm of precipitable water vapor, with essentially no water vapor above or below that layer. Their calculations show that the equivalent pressure (the pressure level with a temperature corresponding to the brightness temperature observed by satellite) was at 463 mb. Because the Norman sounding had 3.0 mm of precipitable water between 600 and 400 mb, and Amarillo had 2.0 mm, the analogy between their idealized result and this real case is quite close. However, the equivalent pressure level would be higher in the real case because the ide-

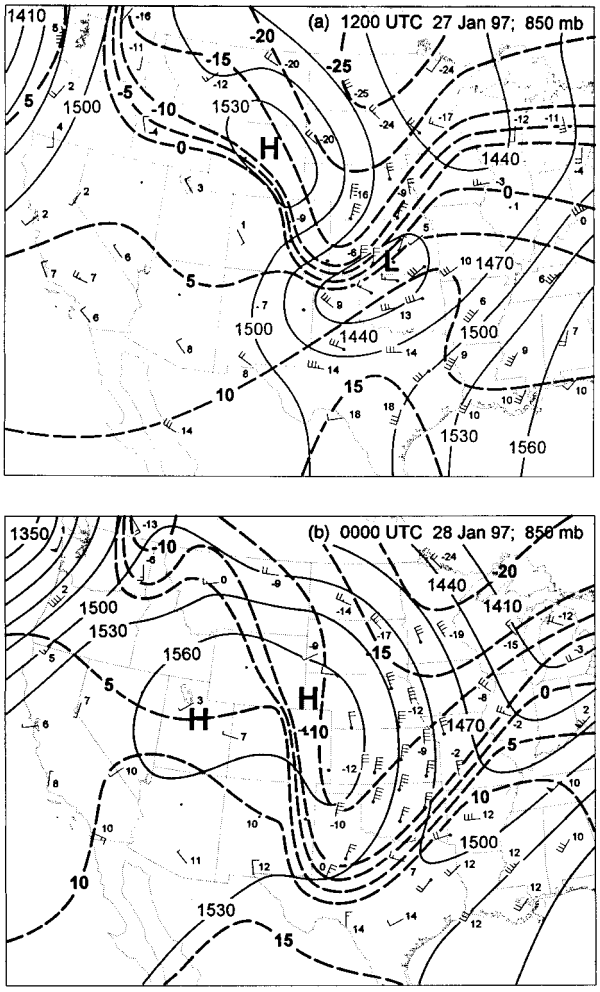

FIG. 5. Geopotential height (m, solid), isotherms (°C, dashed), and winds (as in Fig. 1) at 850 mb: (a) 1200 UTC 27 January 1997 and (b) 0000 UTC 28 January 1997. Wind data from profilers are marked with a solid dot; dots are also shown for the Granada, Colorado, and Tucumcari, New Mexico, profiler sites even though the lowest range gate at each site is above 850 mb.

alized case lacked moisture above and below this layer. Moisture beneath the layer reduces the transmittance of upwelling radiation from lower (warmer) altitudes, while the presence of moisture above provides absorption and emission at higher (cooler) altitudes. This comparison indicates that the waves seen in the water vapor imagery were at altitudes at least as high as 460 mb (or approximately 6.4 km MSL).

Finally, the Norman sounding (not shown) passed

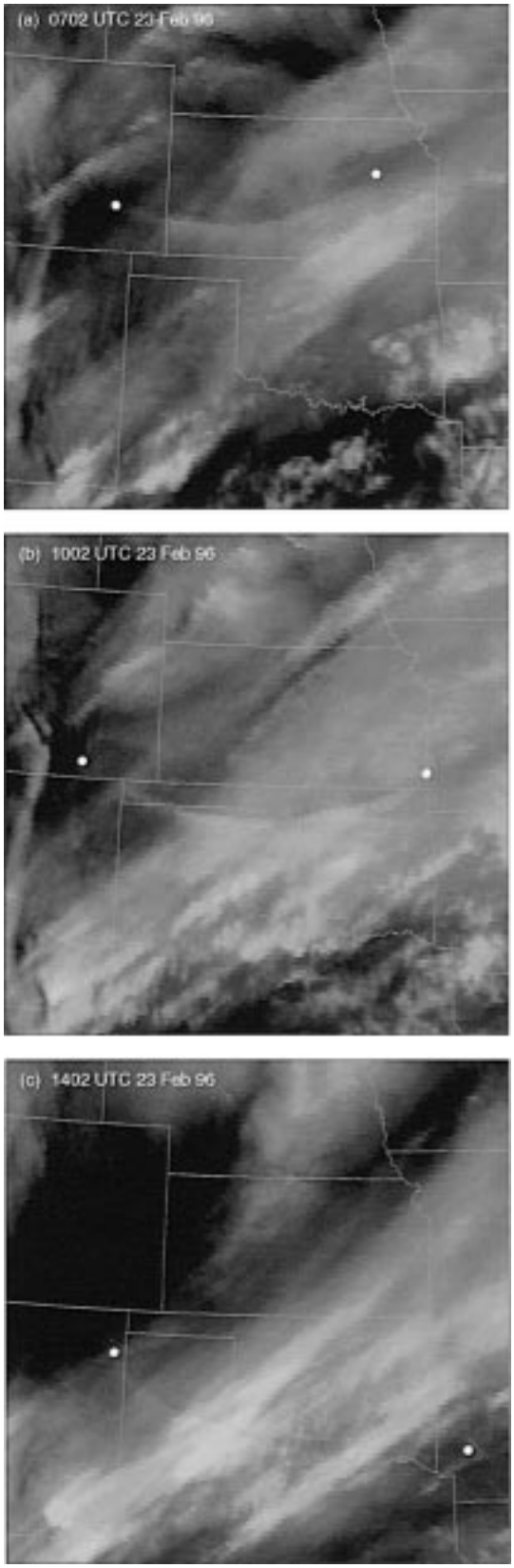

→

FIG. 6. Digitally enhanced water vapor images from *GOES-8* showing the leeside frontal gravity wave on 23 February 1996: (a) 0702 UTC, (b) 1002 UTC, and (c) 1402 UTC. The two large white dots in each image approximately mark the western and eastern ends of the wave perturbation. Note that the wave extends across the southwest-northeast-oriented moist bands and cirrus clouds.

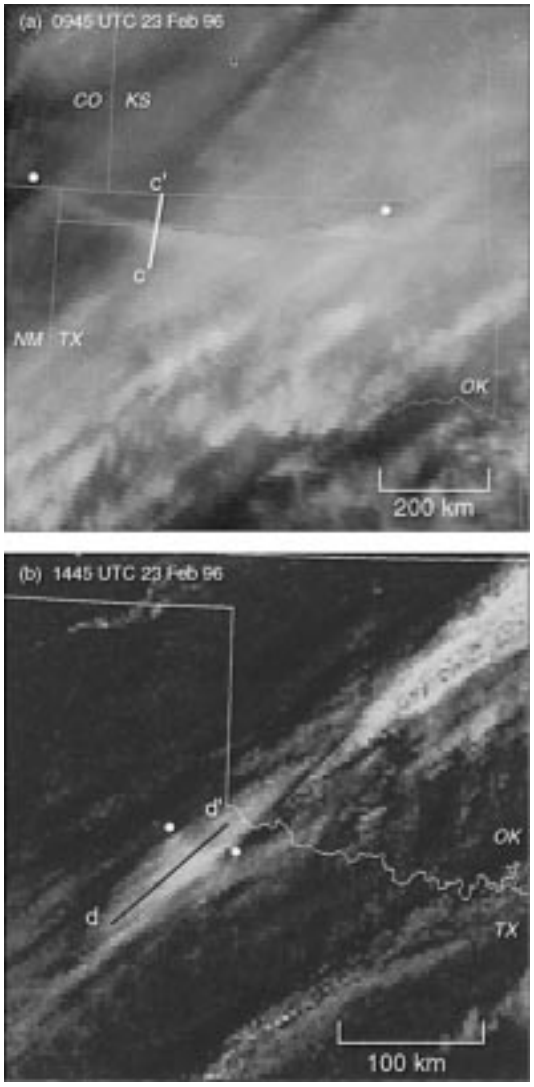

FIG. 7. Digitally enhanced (a) water vapor and (b) visible GOES satellite images of the leeside frontal gravity wave including the baselines (cc′ and dd′) for digital traces shown in Fig. 8. (a) The two large white dots approximately mark the western and eastern ends of the wave perturbation in the water vapor image. (b) The two large white dots mark the western and eastern ends of the wave-perturbed cirrus cloud. Note that the wave extends across the southwest-northeast-oriented moist bands and cirrus clouds.

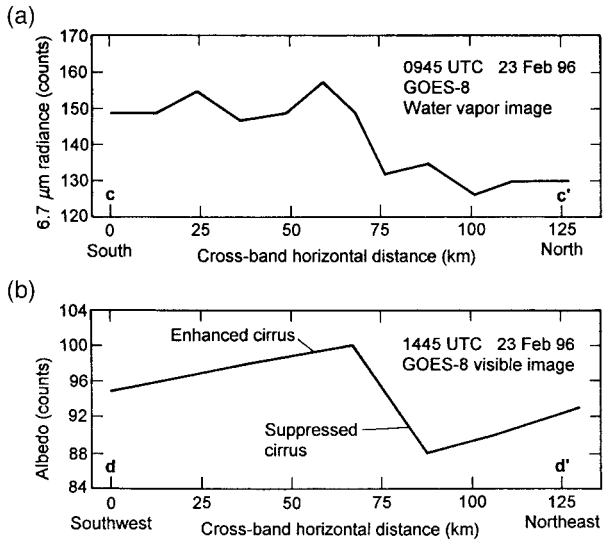

FIG. 8. (a) Brightness of the water vapor image at 0945 UTC on 23 February 1996 along baseline cc′ in Fig. 7a; (b) albedo along line dd′ in the visible image at 1445 UTC shown in Fig. 7b.

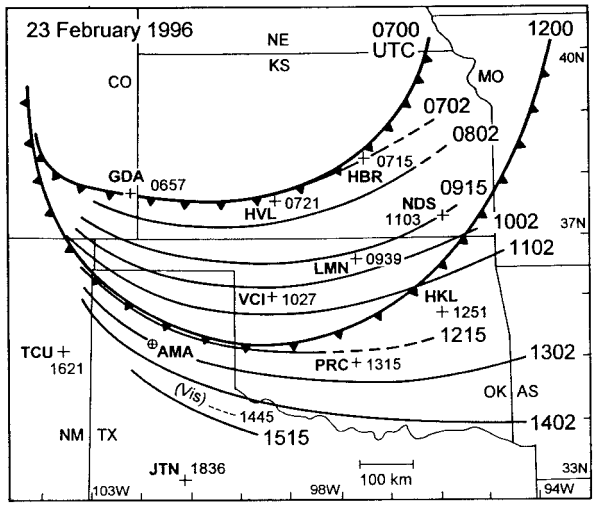

FIG. 9. Isochrone analysis of the position of the leeside frontal gravity wave in water vapor images (solid) and in one visible image (thin dashed, labeled ''Vis'') on 23 February 1996. Regions where the wave was difficult to identify, but still present, in water vapor images are marked by dashed lines. The position of the surface leeside cold front is marked at 0700 and 1200 UTC using cold-frontal symbols. The Amarillo (AMA), Texas, rawinsonde site is marked, as are selected wind profilers [Granada (GDA), Colorado; Haviland (HVL), Hillsboro (HBR), and Neodesha (NDS), Kansas; Tucumcari (TCU), New Mexico; Jayton (JTN), Texas; Lamont (LMN), Vici (VCI), Purcell (PRC), and Haskell (HKL), Oklahoma]. The time of passage of the leeside cold front at the surface at each profiler site is shown based on 6-min sampling (UTC ± 3 min). The arrow near GDA marks the western end of the wave isochrone at 0702 UTC, which is otherwise covered by the frontal symbol.

through a saturated layer from 510 to 440 mb. Because the waves were seen in a cirrus cloud in the region at 1445 UTC (Figs. 7b and 8b), this provides an independent confirmation that the waves produced significant vertical displacements at least as high as the top of this cloud, that is, at least 440 mb, or 6.6 km MSL.

2) WIND PROFILER AND SURFACE OBSERVATIONS OF THE LEESIDE COLD FRONT

The characteristics of the leeside cold front and the prefrontal environment are illustrated by time–height

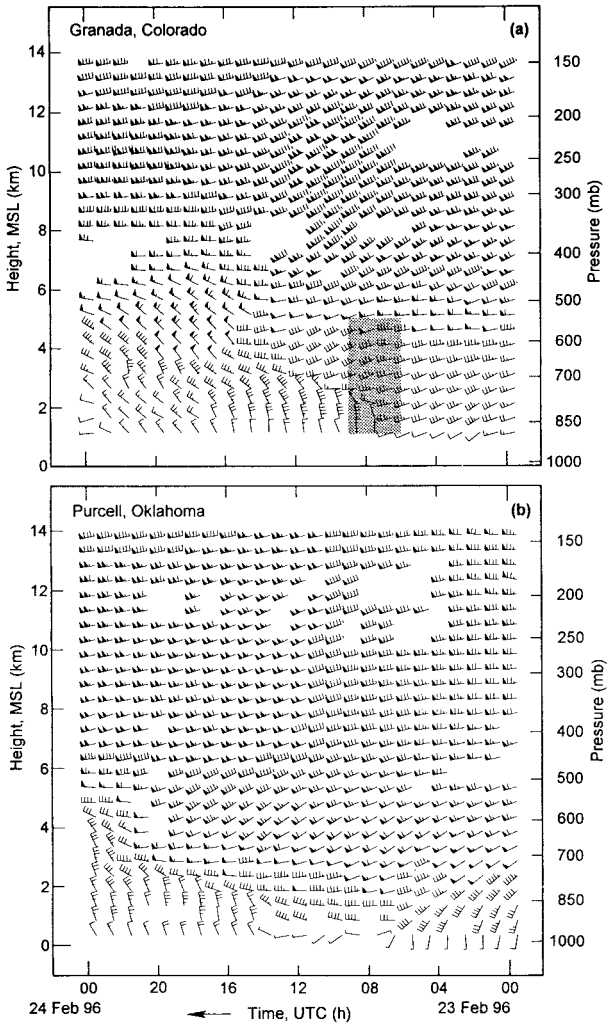

FIG. 10. Time–height sections of hourly consensus-averaged horizontal winds between 0000 UTC 23 February and 0000 UTC 24 February 1996 from (a) Granada, Colorado, and (b) Purcell, Oklahoma. Winds are as in Fig. 1. (a) The shaded area marks the domain of Fig. 11.

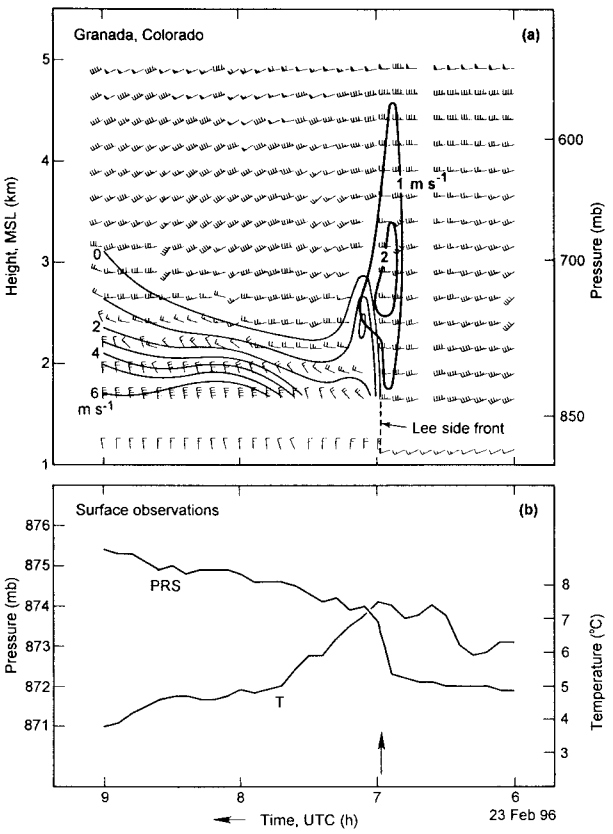

FIG. 11. (a) Time–height section of unaveraged horizontal winds at 6-min time resolution from the Granada, Colorado, wind profiler and surface site (barbs and flags are as in Fig. 1), radial velocities from the north-pointing beam (only values ≥ 0, i.e., northerly, are contoured, thin), and radial velocity from the vertical beam (magnitudes $>|1|$ m s^{-1} are contoured, bold), between 0600 and 0900 UTC 23 February 1996. The dashed line marks the position of the kinematic leeside cold-frontal boundary interpolated between the surface and the lowest radar range gate centered at 500 m AGL; (b) Surface pressure (PRS) and temperature (T) from the same site.

sections of hourly consensus winds from two key wind profilers (Granada, Colorado; and Purcell, Oklahoma) over which the waves passed (Fig. 10). The leeside cold front passed Granada sometime between 0630 and 0730 UTC, as revealed by the wind direction shift from 15 m s^{-1} west-southwesterly to 20 m s^{-1} northerly flow below 3 km MSL. The front passed Purcell between 1230 and 1330 UTC, with a shift from 20 m s^{-1} west-northwesterly to 15 m s^{-1} north-northwesterly flow below 2 km MSL. [The shift from southwesterly to westerly flow at Purcell near 0700 UTC corresponds to the passage of the weak cold front aloft noted earlier (Figs. 1 and 2).] The leeside cold front was marked by a layer of strong vertical directional wind shear representing geostrophic cold advection (Neiman and Shapiro 1989) that moved upward with time from near the surface to 3 km MSL. Although wind observations alone cannot unambiguously identify the position of a frontal zone, a close correlation between the kinematic and thermodynamic frontal zone positions was found by Neiman et al. (1992) using RASS data, and by Neiman et al. (1998) using research aircraft and rawinsonde data. Both the surface and 850-mb thermodynamic analyses (Figs. 1c and 2, respectively), illustrate the cold-frontal temperature gradient (5 K/100 km at 850 mb), and its advection in this case. The surface temperature decreased by 6°–7°C in 1 h at several sites in the area. Rawinsonde ascents from Norman, Oklahoma, and Dodge City, Kansas, show a 15°C temperature difference between the sites at 850 mb for 1200 UTC 23 February. The 850-mb temperature decreased by 18°C at Dodge City over the 12 h ending at 1200 UTC.

The 6-min surface and profiler data from Granada (Fig. 11) reveal the abruptness of the wind shift and pressure rise, and the vertical structure of the leeside cold front and its strong frontal updraft (>2 m s^{-1}); and

pinpoint the time of frontal passage more precisely than do the 1-h-average data. The 6-min sampling shows the surface wind shifted from 6.9 m s^{-1} at 251° to 7.9 m s^{-1} at 5° between 0654 and 0700 UTC. At the same time the station pressure rose 1.3 mb and the surface temperature began a gradual decrease of 2.7°C over 54 min. Based on the 11.9 m s^{-1} phase speed from the isochrone analysis in Fig. 9, these transitions over 6 min correspond to transitions over 4 km horizontally. This front passed at the same time the wave was observed over the site in the water vapor image (Figs. 6a and 9). The profiler-observed radial velocity measured by a beam pointed northward reveals the passage of the leeside cold front as a transition from southerly component to northerly component flow over the lowest 1.5 km AGL during the same time the surface wind shift occurred. Just before this wind shift, the vertically pointing beam of the profiler measured a 2.3 m s^{-1} prefrontal updraft that maximized at the same altitude as the top of the northerly flow (Fig. 11). The horizontal winds calculated from the three profiler beams at 6-min resolution are also shown in Fig. 11, but they may include significant errors near the front due to inhomogeneity between the beams over the 5-min time required for the measurements. Inhomogeneity could result from the horizontal propagation of the narrow wind shift and updraft. Several of the 6-min horizontal winds were clearly in error near the updraft and were deleted. This sampling problem is greatly reduced, but not totally eliminated, by examining the radial velocity from the north beam (Fig. 11), because these measurements each require only a 1-min rather than a 5-min sampling time and assume uniformity within a pulse volume rather than between three beams. [This sampling issue is discussed in Ralph et al. (1995).] Nonetheless, the radial velocities and the 6-min horizontal winds are rather consistent with one another. The profiler wind data also reveal a 0.5-km decrease in the depth of the northerly flow, after the short-lived depth maximum of 2.0 km. This structure is characteristic of a gravity current head.

Under hydrostatic conditions the observed 1.3-mb pressure rise could have resulted from a cooling of 2.1°C over the 1.5-km depth of northerly flow, which is comparable to the observed temperature decrease at the surface. However, recall that the surface cooling occurred over 54 min while the pressure rise took only 6 min. Nonetheless, the rapid pressure rise and wind shift, and the head feature closely resemble the kinematic character of a gravity current. It should also be emphasized that the observed temperature decrease is much slower than would be expected, taking roughly 10 times longer than was seen in other studies of gravity current–like dry cold fronts with similar propagation speeds (e.g., Young and Johnson 1984; Shapiro et al. 1985; Miller et al. 1996). Because two thermometers at the site each measured the same temperature change to within 0.2°C, the gradualness of the temperature decrease, and hence the disparity between the kinematic and thermodynamic structures, is not the result of instrument error.

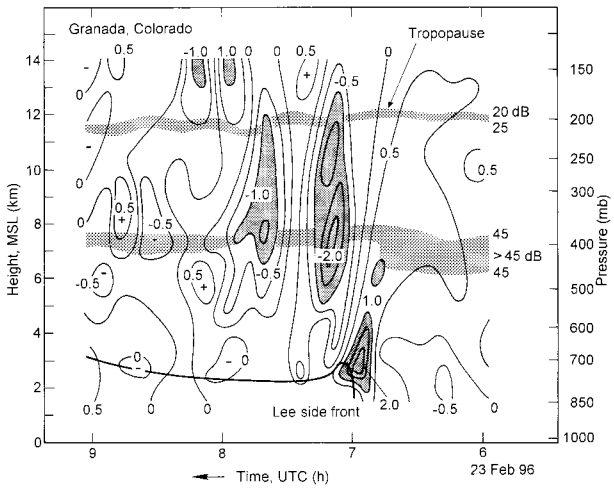

FIG. 12. Radial vertical velocity from the Granada, Colorado, wind profiler (thin solid; magnitudes >|1| m s^{-1} are shaded dark). Two layers of enhanced radar backscatter (dB) from the clear air are also shown (light shading), including one that approximately marks the tropopause. The frontal position (bold) is based on Fig. 11.

3) WIND PROFILER OBSERVATIONS OF DEEP-TROPOSPHERIC GRAVITY WAVES AT GRANADA, COLORADO

The wind profilers at Granada, Colorado, and Purcell, Oklahoma, each provided direct observations of gravity waves in the middle and upper troposphere associated with the surface leeside cold front. As has been established by Ralph et al. (1992, 1993a,b, 1997) and Worthington and Thomas (1996), such wind profiler vertical velocity time series can be used to determine wave vertical structure. The vertical-beam radial velocities, which represent clear-air vertical motions in the observed conditions where precipitation was absent, are shown in Figs. 12 and 13. The waves are highlighted in Fig. 12 using hand-drawn contours of vertical motion, while Fig. 13 uses stacked time series. At Granada (Fig. 12) the data reveal a forward-sloping updraft of 0.5–1.0 m s^{-1} above the frontal updraft. Evidence of this updraft is also seen in the vertical displacement of a layer of enhanced signal power between 6 and 8 km MSL. This is followed in the same layer by a primary downdraft of >2 m s^{-1}, a weak updraft, and another downdraft. These perturbations had a ground-relative period of 30 min. The waves trailing the leading updraft were vertically oriented, suggesting that the waves were trapped. The downdrafts in the 6–8-km layer are also associated with slight downward displacements of the same layer of enhanced signal power that had earlier been lifted. The magnitude of the downward displacement (~500 m) is, however, less than expected (>1 km based on the strength and duration of the downdrafts).

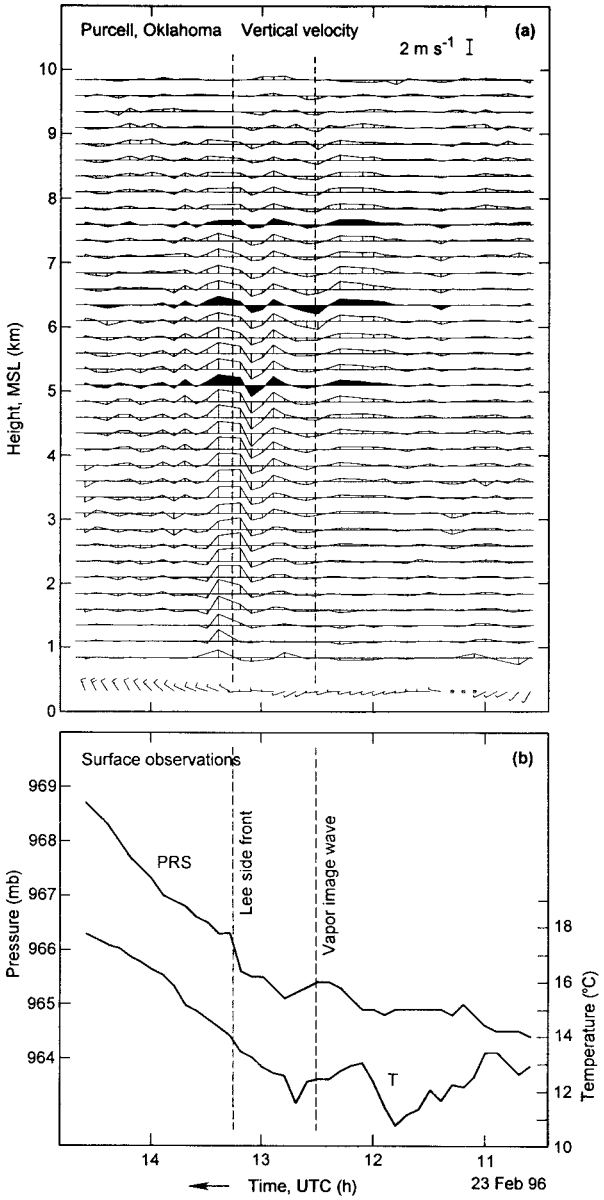

FIG. 13. (a) Time–height section of 6-min-resolution radial vertical velocity (scale at upper right) from the Purcell, Oklahoma, wind profiler, and surface winds (as in Fig. 1) from the same site, between 1036 and 1436 UTC 23 February 1996. Data from the longer-pulse ''high'' mode are used above 7.7 km, while data from the short-pulse ''low'' mode are used below that. Shading of data at 5.1-, 6.4-, and 7.6-km highlights the midtropospheric gravity waves. (b) Surface temperature and pressure traces from the same site. Vertical lines mark the time of the leeside surface cold frontal passage, and the time of the passage of the node of the leading wave seen in the water vapor images.

This difference suggests that other processes, such as modification of turbulence by the strong wave activity, most likely dominated the temporal evolution of scattering in this layer, rather than just pure vertical advection. In contrast, a layer of enhanced backscatter near 12 km MSL, which roughly marks the tropopause (the tropopause was at approximately 12 km MSL in rawinsonde data at 1200 UTC; Fig. 21), shows vertical deflections that are very closely in phase with the vertical motions observed in the same layer. This suggests that the observed vertical deflections could be interpreted as vertical displacements. Thus there is evidence that the surface leeside cold front forced strong gravity waves in the middle and upper troposphere and caused ripples on the tropopause having roughly 700-m vertical displacements. These perturbations also extended into the lower stratosphere.

Recall that the wave in the water vapor images was collocated with the surface leeside cold frontal passage to within a few minutes at Granada. Thus, the strong vertical motions observed by the profiler were in the same layer that the water vapor channel and the visible image were observing [i.e., 440 mb (6.6 km MSL) or higher], which establishes that the southward-propagating perturbations in the water vapor images over Granada resulted from gravity waves forced by the surface leeside cold front. This is consistent with the interpretations based solely on the collocation of the surface leeside cold front and the satellite perturbations within the middle and upper troposphere in the western segment of the domain where the waves were observed (Fig. 9). However, recall that Fig. 9 also showed that the wave was ahead of the front at positions farther east. This interesting behavior is documented in the next section.

4) OBSERVATIONS OF PREFRONTAL DEEP-TROPOSPHERIC GRAVITY WAVES

Comparison of the isochrone analysis of the satellite-observed wave and the leeside cold front (Fig. 9) indicates that Purcell, Oklahoma, was in a region where the wave passed overhead at roughly 1230 UTC 23 February 1996, 45 min before the surface front arrived at 1315 ± 3 min UTC (Fig. 13). The surface front was marked at that site by a shift from westerly to northwesterly winds and a 0.7-mb pressure rise between 1312 and 1318 UTC. The absence of a distinct temperature change may have been due to diurnal heating shortly after sunrise. The timing of this frontal passage is in close accord with that extrapolated from Fig. 9 on the basis of the frontal positions at 0700 and 1200 UTC.

A time–height section of vertical radial velocity from the Purcell wind profiler (Fig. 13a) reveals distinct upward vertical motions from roughly 3 to 9 km MSL beginning at 1150 UTC and ending when the satellite imagery showed the primary wave passing overhead at about 1230 UTC. The upward vertical motions reached 1 m s^{-1} at 6.7 km MSL. The absence of a change of phase with height indicates that this wave was vertically trapped. Vertical velocity disturbances with similar amplitudes and vertical structure, but shorter ground-relative periods and larger amplitudes, followed the first

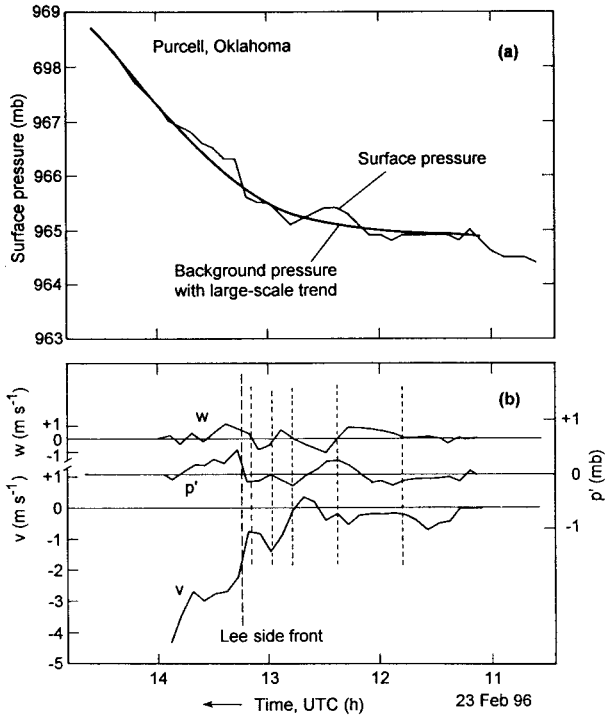

FIG. 14. (a) Time series of surface pressure (thin) and subjectively interpreted background pressure trend (bold) from the Purcell, Oklahoma, wind profiler site. (b) Vertical radial velocity (i.e., vertical air motion) from 6.4 km MSL (w, m s^{-1}), surface pressure perturbation (p', mb) determined from the difference between total and background surface pressures in (a), and wave-normal (N = 340°) surface wind speed (v, m s^{-1}) at Purcell. The long-dashed vertical line marks the surface leeside cold-frontal passage. The short-dashed vertical lines mark times of zero vertical air motion at 6.4 km MSL.

disturbance until the surface front passed with its 1.5 m s^{-1} updraft.

Close examination of the surface pressure trace in Fig. 13b suggests that weak but coherent perturbations were superposed on a rather smoothly varying background pressure increase. This is illustrated in Fig. 14a, which shows an estimate of this background pressure trace. The differences between the total and estimated background pressures, P', are shown in Fig. 14b. The wave-normal surface wind speed is also plotted, as is the vertical velocity from a representative altitude of 6.4 km MSL. Comparison of these variables before the leeside cold-frontal passage and pressure rise shows the phase relationship expected for a train of trapped gravity waves where the pressure perturbation trails the vertical motion by 90° (Ralph et al. 1993a). Although the wave-normal surface wind component shows some evidence of being in phase with the pressure perturbation, as expected for such a wave, the agreement is less robust. It is important to note that the pressure perturbation amplitude is 0.2–0.3 mb, while the wave-normal surface wind perturbation amplitude is $<$0.5 m s^{-1}. The small amplitude of the velocity perturbation suggests that minor flow variations resulting from other phenomena could easily mask the wave perturbation.

The consistency of the observations of a perturbation seen in satellite water vapor images, profiler-observed vertical motions, and surface perturbations provides a uniquely complete view of a prefrontal gravity wave containing mid- and upper-tropospheric vertical motions of up to 1 m s^{-1}. The wave precedes the front by at least 45 min at this site, which, using a representative frontal phase speed of 14 m s^{-1}, indicates a minimum distance of 37 km ahead of the front. This distance matches the estimated distance of 37 km between the wave in satellite imagery and the front at 1215 UTC (Fig. 9) in the front-normal direction and is close to the 50 km distance in the wave-normal direction. Because the data at Purcell confirm the initial impression from Fig. 9 that the satellite-observed wave is ahead of the front east of the Haviland, Kansas, profiler site, it is concluded from Fig. 9 that the wave was up to 150 km ahead of the front in eastern Oklahoma.

b. The 27 January 1997 case

1) SATELLITE OBSERVATIONS OF GRAVITY WAVES

A second event, which occurred on 27 January 1997 over Texas, is shown here to illustrate the gravity wave behavior in a case characterized as an arctic leeside cold front and to demonstrate the repeatability of key aspects of the leeside frontal gravity waves. The synoptic environment was shown in section 3c, which included a surface frontal analysis and satellite water vapor image at 2100 UTC (Fig. 4). The wave was clearly evident from 1730 to 2045 UTC (Figs. 15 and 16) but was subtle before that. At 1500–1530 UTC a weak band of brightening in a water vapor image stretched across the Jayton, Texas, profiler (not shown). From 1730 to 1930 two bands were present in the eastern part of the disturbance (Fig. 15). The first band (marked ''c'' in Fig. 15) decayed while the second one (marked ''b'') became more distinct during this period. The bands intersected at a longitude west of Jayton, and this intersection moved southward.

2) WIND PROFILER AND SURFACE OBSERVATIONS OF THE LEESIDE COLD FRONT

Hourly averaged surface and profiler observations from Jayton reveal that the leeside cold front occurred between 1430 and 1530 UTC from the surface to 2.5 km MSL (Fig. 17). It is marked by a shift from 3 m s^{-1} westerly flow to 5 m s^{-1} northerly flow at the surface. The profiler shows a shift from 15–20 m s^{-1} northwesterly to 10–15 m s^{-1} north-northwesterly up to 2.5 km MSL between 1500 and 1600 UTC, and to northerly and northeasterly by 1700 UTC. By 2300 UTC the north-northeasterly winds in the lowest 1 km AGL had reached 12 m s^{-1}. An earlier (1100–1500 UTC), gradual

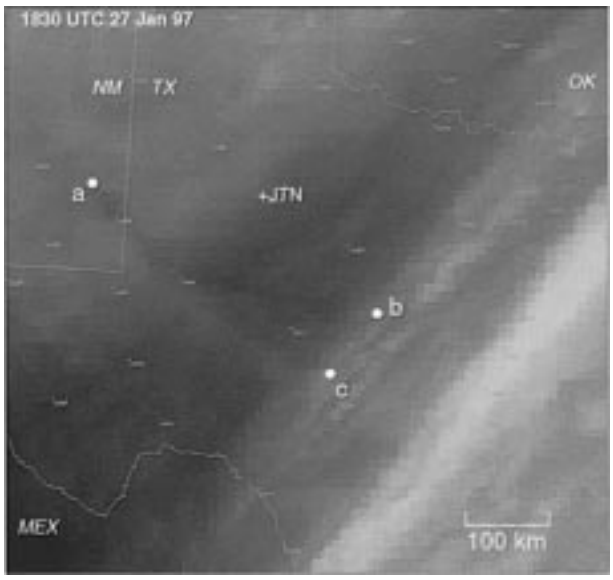

FIG. 15. Digitally enhanced water vapor image from *GOES-8* on 27 January 1997, showing the leeside frontal gravity wave with multiple bands. The large white dot labeled ''a'' marks the western end of the wave perturbation. Southeast of ''a'' the single band splits into two bands, each of which is marked at its eastern end by a large white dot (labeled ''b'' and ''c''). The Jayton, Texas, profiler site is shown (JTN).

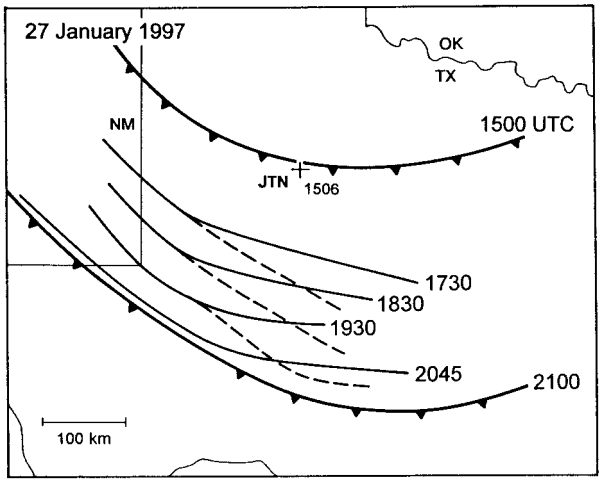

FIG. 16. Isochrone analysis of the position of two waves observed in water vapor images (thin solid, and dashed lines). The position of the surface leeside cold front is marked at 1500 and 2100 UTC 27 January 1997 using cold-frontal symbols. The time of passage (UTC) of the leeside cold front at the Jayton (JTN), Texas, profiler site is given (UTC).

shift from southwesterly to westerly at the surface and from westerly to northwesterly in the lowest 2 km AGL closely resembles the prefrontal turning observed at Purcell, Oklahoma, during the 23 February 1996 case described in section 4a (Fig. 10b). This shift is most likely due to the passage of a weak cyclonic disturbance seen in Fig. 5a.

A more detailed view of the frontal passage using 6-min data from Jayton is given in Fig. 18, which can be compared with similar data from the 23 February 1996 case in Fig. 11. A 7°C temperature drop between 1536 and 1542 UTC (Fig. 18b) corresponds to a surface wind shift from north-northwesterly to north-northeasterly (Fig. 18a). However, the >1 m s^{-1} frontal updraft and low-level convergence are found with a wind shift that occurred 30–36 min earlier, between 1500 and 1512 UTC (Fig. 18a). This wind shift occurred from the surface to 3 km MSL and was marked aloft by a 20° wind direction shift within 15–20 m s^{-1} northwesterly flow. The 6-min radial velocities from the north-pointing beam (oriented at 349°) reveal a significant wind speed increase along that direction, followed by an even greater decrease. This pattern creates a kinematic headlike feature resembling a gravity current, but as with the earlier case, the thermodynamic changes differ from classic gravity current behavior. This disparity between the thermodynamic and kinematic frontal structures resembles the prefrontal northerly acceleration in leeside fronts described recently by Bluestein (1993), Colle and Mass (1995), and Hutchinson and Bluestein (1998) as resulting from horizontal advection of a lee trough. A similar, though shorter (10 min), disparity was also shown by Hobbs and Persson (1982) for fronts on the Pacific coast. It may also be possible that the disparity results from a prefrontal bore. It is also interesting that the updraft and downdraft are correlated with a relative increase and then decrease in surface pressure. Such a correlation is consistent with hydrostatic pressure changes created by the vertical motions, just as was observed in the prefrontal gravity waves at Purcell, Oklahoma, during the 23 February 1996 case (Fig. 14).

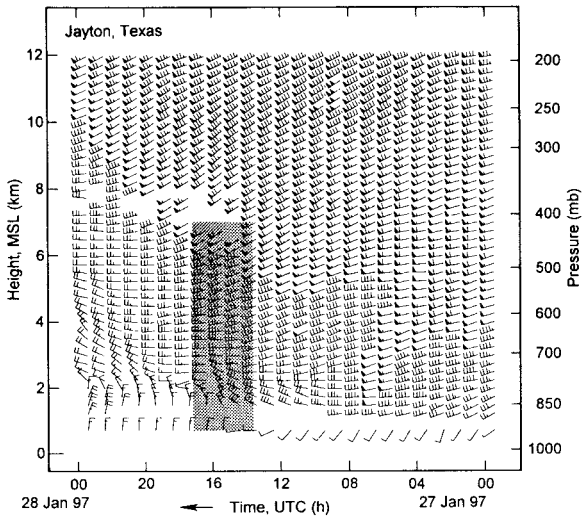

FIG. 17. Time–height section of hourly consensus-averaged horizontal winds from Jayton, Texas, on 27 January 1997. Winds are as in Fig. 1. The shaded area marks the domain of Figs. 18 and 19.

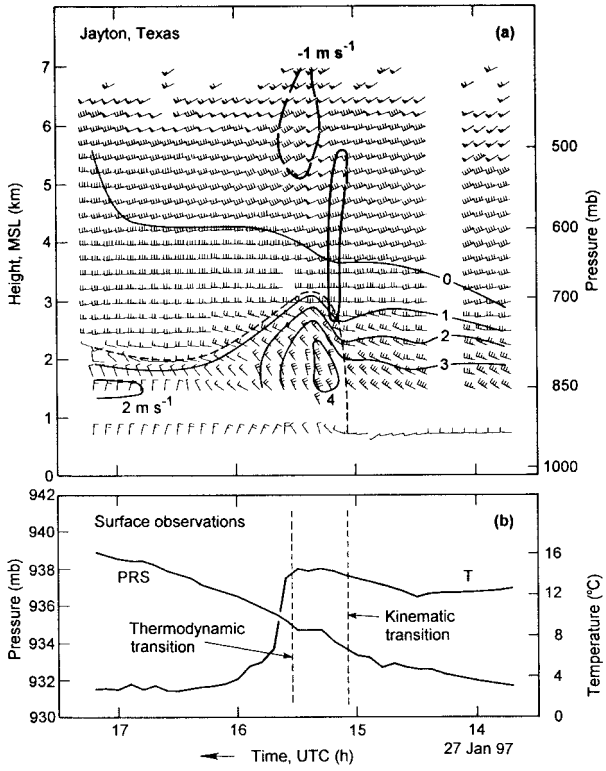

FIG. 18. (a) Time–height section of unaveraged horizontal winds at 6-min time resolution from the Jayton, Texas, wind profiler, and surface site (barbs and flags are as in Fig. 1), 6-min radial velocities from the north-pointing (349°) beam (only values ≥0, i.e., northerly, are contoured, thin), and radial velocity from the vertical beam (magnitudes >|1| m s^{-1} are contoured, bold), between 1342 and 1712 UTC 27 January 1997. (b) Surface pressure and temperature from the same site. The kinematic frontal boundary is marked aloft with a thin dashed line in (a), as are the times of the themodynamic and kinematic transitions at the surface in (b).

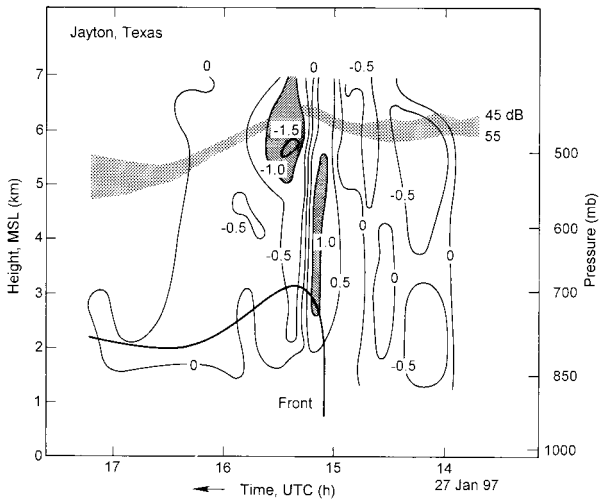

FIG. 19. Radial vertical velocity from the Jayton, Texas, wind profiler (thin, solid; magnitudes >|1| m s^{-1} are shaded dark). A layer of enhanced vertical gradient of radar backscatter (dB) from the clear air is shown (light shading). The frontal position (bold) is based on Fig. 18.

3) WIND PROFILER OBSERVATIONS OF DEEP-TROPOSPHERIC GRAVITY WAVES AT JAYTON, TEXAS

As with the earlier case, strong vertical motions were observed above and ahead of the front (Fig. 19).[1] The narrow updraft between 1500 and 1512 UTC is maximized near the top of the head of the kinematic frontal boundary at 3–4 km MSL. This is followed by a downdraft of 1.5 m s^{-1} centered near 6 km MSL. This updraft–downdraft pair resembles the observations from Granada, Colorado, in the earlier case (Fig. 12). Weaker backscatter from the upper troposphere and lower stratosphere in this case, however, does not allow for measurements up to 14 km MSL as was possible in that case. Temporal changes in the altitude of a layer of strong vertical gradient of signal power observed at 5–6 km MSL (Fig. 19) match rather closely the vertical motions observed in that layer. Note that the upward displacement of the layer near the top of the updraft is followed by a downward displacement beginning within 6 min of the time downward motion was observed in the layer at about 1518–1524 UTC. The inferred vertical displacements are roughly 350 m up followed by 1.1 km down. Calculation of the vertical displacements expected due to the observed vertical motions in the same layer agree in sign, but only to within a factor of 2 (i.e., 540 m up in 18 min, followed by 2.0 km down in 48 min). This assumes that the layer is modified only by vertical displacements of a steady-state vertical circulation (quite likely due to a gravity wave). This assumes that no other processes, such as modulation of turbulence by the vertical motions, are modifying the signal power distribution. Given that gravity waves are known to modulate turbulence through wave-induced changes in the Richardson number, this assumption could be invalid. This could explain the mismatch between the observed vertical displacement of a similar layer of strong signal power near 7 km MSL in the earlier case and why the agreement is good at other times, for example, near 12 km in the earlier case (Fig. 12).

4) OBSERVATIONS OF PREFRONTAL DEEP-TROPOSPHERIC GRAVITY WAVES

Satellite images from this case show two main banded perturbations between 1730 and 1930 UTC (Figs. 15 and 16). Because the features in the satellite imagery are very subtle before that time period it is not possible

[1] For this case the leading edge of the front will be defined by the primary kinematic boundary that passed between 1500 and 1512 UTC, because it is associated with the major updraft. However, it should be noted that this feature may itself have been part of a prefrontal bore, and the true front would be better defined as the thermodynamic boundary that passed 30–36 min later.

to directly trace the perturbations back to the time they would have passed over the profiler site at Jayton, Texas. However, extrapolation of the positions of these features backward from 1730 to 1506 UTC indicates that the first, or southernmost, band is ahead of the surface front (kinematic boundary), and that the second band is roughly coincident with the front. This is supported by the 1500 UTC surface-frontal position (Fig. 16).

The average spacing between the two bands along a north–south line through Jayton is 38 km, and the southward frontal motion is 11.7 m s^{-1}. Thus, the first band would have passed Jayton 55 min before the front. The vertical velocity data from Jayton (Fig. 19) reveals a vertically oriented region of downward motion from 1.0 to 6.5 km MSL, centered on 1412 UTC. (It should be noted that this is during an 18-min data gap but that the good data on each side of this gap reasonably justified the interpolation required to create the continuous analysis shown in Fig. 19.) This downdraft has a magnitude of >0.5 m s^{-1} and is the second strongest feature in the data, only weaker than the main feature near 1512 UTC. Thus, both satellite imagery and profiler data show a gravity wave ahead of the kinematic surface front by 1 h, or 40 km.

5. The gravity wave–generation mechanism

a. Observed correlation between the gravity waves and front-relative cross-front flow

Previous studies have shown that gravity waves can be created by flow across an atmospheric obstacle such as undulations atop the convective boundary layer (Clark et al. 1986; Kuettner et al. 1987), the leading edge of a gravity current (Ralph et al. 1993b; Jin et al. 1996), a cold front in Colorado (Neiman et al. 1995), and the top of deep convection (Fovell et al. 1992). Also, Snyder et al. (1993) concluded that the weak gravity waves created during frontogenesis simulations arose as the linear forced response to cross-front accelerations. These observational, theoretical, and modeling results suggest that the deep-tropospheric gravity waves found here in association with the leeside cold fronts could have resulted from the front acting as an obstacle to cross-front flow. We describe below how the prefrontal cross-front flow in a front-relative sense was amplified because the blocking effects of the mountains changed the frontal orientation.

Using the wind profiler data from the sites over which the leeside cold front and gravity waves passed during the 23 February 1996 event, the prefrontal front-relative, cross-front wind speed (i.e., the component normal to the front) at each site is documented. This calculation requires knowledge of the frontal orientation and propagation speed at each profiler site. The frontal orientation at 1200 UTC 23 February is shown in Figs. 1 and 9 and is based on analysis of surface data presented in Fig. 1 and on profiler data presented in section 4a.

TABLE 2. Characteristics of the leeside cold front and prefrontal winds observed by radar wind profilers during the 23 February 1996 leeside frontal gravity wave event. The frontal orientation is derived from the surface frontal analyses shown in Figs. 1 and 9 (Fig. 9 shows site locations). The prefrontal, front-relative, cross-front wind speed is an average of the hourly consensus-averaged winds over the four range gates in the layer from 0.5 to 1.25 km AGL during the hour before frontal passage. Here x is the distance east of 105° W; θ the frontal orientation (° from north); V the prefrontal, ground-relative, cross-front wind speed; c_f the ground-relative phase speed of surface front; V_r the prefrontal, front-relative, cross-front wind speed.

Site name	x (km)	Altitude (m, MSL)	θ (°)	V (m s^{-1})	c_f (m s^{-1})	V_r (m s^{-1})
GDA	247	1155	35	13.8	8.7	22.5
VCI	519	648	350	−1.8	14.2	12.4
HVL	519	648	350	−1.2	15.0	13.8
LMN	669	306	335	−8.9	9.4	0.5
HBR	671	446	325	−10.2	12.1	1.9
PRC	680	331	340	−13.5	14.0	0.5
NDS	826	254	315	−9.7	9.2	−0.5
HKL	830	219	315	−8.9	10.6	1.7

To calculate the frontal motion, another surface frontal analysis was performed for 0700 UTC. The frontal position at this time (Fig. 9) is pinned down well by 6-min surface and profiler data at Granada, Colorado, and Haviland and Hillsboro, Kansas. The frontal orientation and propagation speed normal to the front are given in Table 2 for eight profilers. The prefrontal ground-relative cross-front wind speed was determined for each site by averaging this wind component in the lowest four range gates (i.e., from 0.5 to 1.25 km AGL) using the 1-h consensus-averaged winds during the hour before the front passed. This height range is used because it is roughly the depth of the leading edge of the front, and surface data are excluded due to friction. The hourly average is used rather than 6-min data to reduce noise. The prefrontal cross-front wind speed in a front-relative sense (V_r) was determined by subtracting the frontal motion from the vertically averaged prefrontal cross-front flow. These results are also shown in Table 2.

The parameter V_r is shown in Fig. 20 as a function of distance east of the mountains, which is taken here as 105°W. It drops from 22.5 m s^{-1} at Granada, to approximately 13 m s^{-1} at Haviland and Vici, and finally to <2 m s^{-1} at sites farther east. This variation results primarily from the changes of the orientation of the front but is also affected by variations of the prefrontal wind direction. These lead to a ground-relative cross-front flow that changes sign from >10 m s^{-1} positive (warm to cold) in the west, to roughly -10 m s^{-1} (cold to warm) farther east. Because the frontal propagation opposed this flow near the mountains, V_r was amplified, while farther east the frontal propagation roughly compensated for the cross-front flow, resulting in small values of V_r. As should be expected, the frontal propagation speed is fastest along an axis parallel to the mountains where it surged southward (Fig. 9 and Table 2).

Comparison of V_r with the satellite imagery of 23

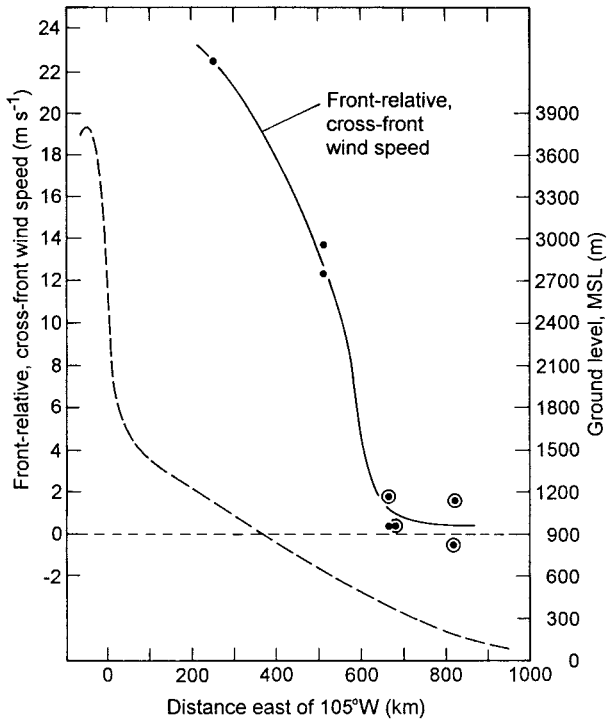

FIG. 20. Layer-averaged prefrontal, front-relative, cross-front wind speed V_r (m s^{-1}; solid line; >0 is prefrontal flow toward the front) for the four lowest range gates (i.e., 0.5–1.25 km AGL) from eight wind profiler sites (described in Table 2) on 23 February 1996 as a function of the site's distance from the mountains (approximated by the 105°W meridian). The dots mark actual data points, and the curve represents an approximate best fit to the data. Sites that were near the eastern end of the discernible water vapor perturbation in satellite images are noted by a circle. Also shown is the mean ground profile (m; dashed line) based on the altitudes of the eight profiler sites, and the surface farther west.

February 1996 indicates that the three sites with large V_r coincided with sites where the satellite imagery and frontal analysis showed a well-defined wave or wave train in the water vapor imagery that was essentially collocated with the leading edge of the surface leeside cold front. In contrast, the sites with relatively weak V_r were at positions where the satellite frontal comparison indicates that the wave or wave train was measurably ahead of the front, and these sites were also near the eastern edge of where the waves were discernible in the satellite imagery (Fig. 9). This comparison supports the hypothesis that the gravity waves were forced by the strong prefrontal cross-front, front-relative flow, as would be expected if they were created by the obstacle effect. However, this seems counter to the observation that the waves were ahead of the front at eastern sites, a point that is examined in the next section.

It should also be noted that the frontal updraft, which is the flow feature that directly forces the gravity waves, is due to convergence between the postfrontal and prefrontal front-normal flow. In contrast, the obstacle effect results purely from the convergence of the prefrontal front-normal flow with the front and thus neglects the contribution from the postfrontal flow.

b. The gravity wave environment

Because gravity waves can be trapped vertically under certain conditions, the wave energy can propagate horizontally far from its original source. In the case of mountain-generated trapped lee waves, it has traditionally been considered that their ground-relative horizontal phase speed is zero, and their group velocity transmits the wave downstream of the mountains. Recent observational (Ralph et al. 1997) and idealized (Nance and Durran 1997) studies have shown, however, that trapped lee waves can become nonstationary with respect to the mountain; that is, they have a nonzero ground-relative horizontal phase speed. When the background flow changes with time, the original group velocity can even result in their propagation to the upstream side of the obstacle that originally forced them (Nance and Durran 1997).

This type of nonstationarity appeared to have occurred as the leeside cold front surged south. The southward acceleration of the front near the mountains changed the orientation of the front relative to the background flow. This occurred in a way that decreased V_r with time, following a segment of the front that connected the relatively unperturbed portion of the front to the northeast in Missouri and Iowa with the portion surging southward in eastern Colorado and western Kansas. This frontal segment rotated with time from an orientation of roughly northeast-southwest to north-northeast–south-southwest (Fig. 9). In the event on 23 February 1996 the orientation changed from 52° east of north to 38° east of north in 5 h. This is based on a frontal segment that passed over Hillsboro, Kansas, near 0700 UTC. The position of this segment of the front at 1200 UTC was determined by the intersection of the front-normal direction at 0700 UTC with the front at 1200 UTC (Fig. 9). The rotation began in southern Nebraska and northern Kansas as the blocking effects of the highest mountains came into play. Such rotation is seen in other studies of leeside cold fronts in the area [Colle and Mass (1995), rotated 15° between 0000 and 1200 UTC 12 November 1986; Hutchinson and Bluestein (1998), rotated 30° between 0000 and 1800 UTC on 29 October 1993; Neiman et al. (1998), rotated 60° between 0000 and 1800 UTC 9 March 1992]. This rotation is a geometric consequence of a leeside cold surge.

To explore the wave propagation environment and the waves it would support, the vertical profile of the Scorer parameter l was calculated from a well-placed sounding in the immediate prefrontal environment at Amarillo, Texas, at 1200 UTC 23 February 1996 (Fig. 21). This sounding is used to initialize a numerical simulation. The square of the Scorer parameter (e.g., Scorer 1949;

Smith 1979), including the curvature term ($\partial^2 V_r/\partial z^2$), is given by

$$l^2 = (N/V_r)^2 - (1/V_r)\partial^2 V_r/\partial z^2, \quad (1)$$

where z is altitude; V_r is prefrontal, front-relative, cross-front wind speed; and N is the Brunt–Väisälä frequency. The l^2 profile (Fig. 21c) is valid 1 h before the wave and leeside cold front passed Amarillo (Fig. 9). Because the balloon wind data were missing above 500 mb, hourly consensus-averaged winds above 500 mb from the wind profiler at Vici, Oklahoma, were used above that level. The profiler data were from 1030 UTC to account for the motion of the front. The Scorer parameter profile was derived using V_r (Fig. 21b), assuming a frontal motion at Amarillo of 11.3 m s^{-1} from 20° (Fig. 9). Both the temperature and winds were interpolated to a vertical resolution of 250 m to match the vertical grid used in a numerical simulation of the event, described in the next section. Because no critical level was present for a gravity wave that had a ground-relative phase speed equal to the front's ground-relative motion (Fig. 21b), reflection from a critical level could not have trapped the waves. However, the mean decrease of l^2 with height over the layer from 1–10 km MSL (Fig. 21c), or the rapid increase of l^2 with height at the tropopause could have caused gravity wave trapping (e.g., Scorer 1949; Smith 1979; Crook 1988; Ralph et al. 1992). The layer of $l^2 < 0$ between 9 and 10 km MSL would also act to trap wave energy, but these negative values result from the small changes in V_r with height that cause a large contribution from the curvature term. Such large values of the curvature term can result even from layers that are too small to have a significant impact on such a deep gravity wave and thus may be spurious. These uncertainties are reduced, however, by using a fully nonlinear, nonhydrostatic numerical simulation presented in the next section. The profiler-observed vertical velocities indicate that the waves were characterized by vertical phase lines, which is an attribute of trapped waves, and thus supports the conclusion that the wave environment favored wave trapping (Ralph et al. 1992).

Although the two-dimensionality assumption seems well-justified here, the front is curved, and the wave environment changes along the front. The latter point is highlighted by Fig. 20 and Table 2, where V_r is shown

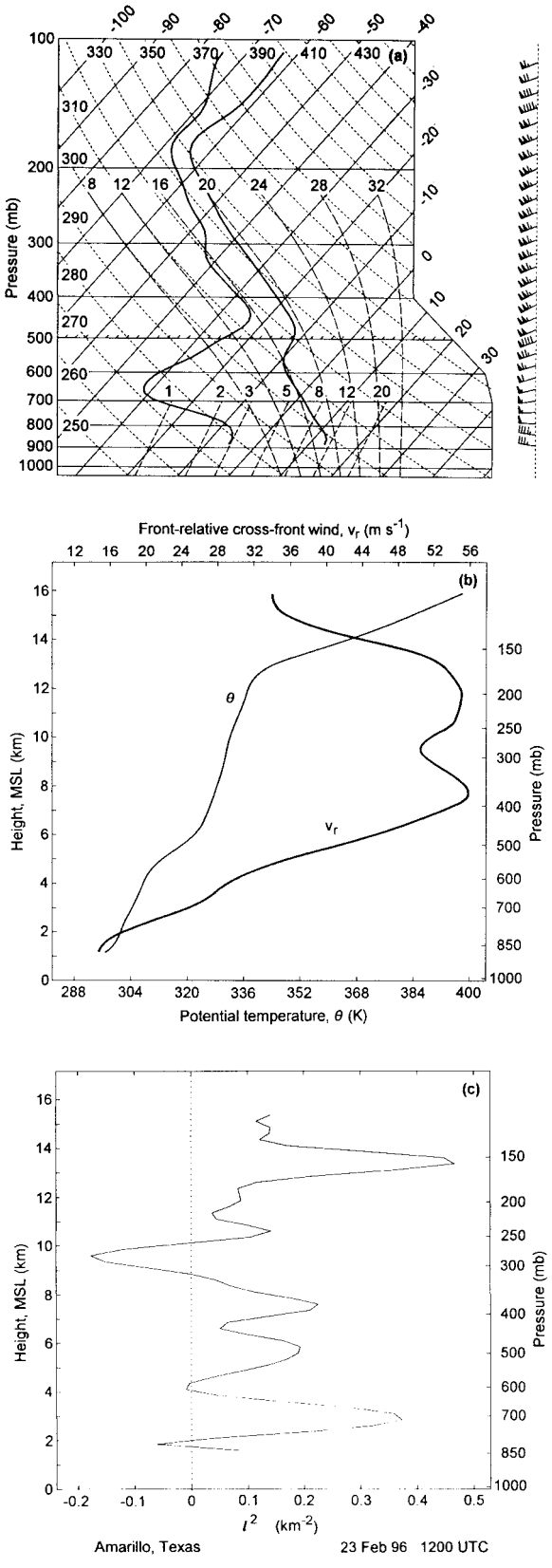

→

FIG. 21. Prefrontal sounding from Amarillo, Texas, at 1200 UTC 23 February 1996. The 1-h consensus-averaged winds from the Vici, Oklahoma, wind profiler valid at 1030 UTC were used above 500 mb where the balloon wind data were missing. All data were smoothed to a uniform spacing of 250 m for use in initializing a numerical simulation (see Fig. 22). (a) Skew-T–log$p$ profiles of temperature and dewpoint temperature. Horizontal winds are shown using the notation of Fig. 1. (b) Front-relative cross-front wind speed (m s^{-1}, thick) and potential temperature (K, thin). The frontal motion used was 11.3 m s^{-1} from 20°. (c) Vertical profile of the square of the Scorer parameter from Eq. (1) based on the profiles in (b).

to vary substantially along the front. The full vertical profiles of V_r, from which the data for Table 2 and Fig. 20 were extracted, indicate that the vertical shear profile also changes significantly along the front (not shown). This is primarily a result of the change in the frontal orientation and propagation. The changes indicate that the wave environment shown in Fig. 21 and used to initialize the numerical model may be substantially different from the environment east of Haviland, Kansas, and Vici, Oklahoma. Thus, these results may not apply to regions where the wave appears ahead of the front. Recall, however, that the direct observations of the wave vertical structure at Purcell, Oklahoma, did indicate the observed waves were trapped [section 4a(4)].

c. A numerical simulation assuming the front acted as an obstacle

To more accurately explore the wave environment and the hypothesis that the obstacle effect of the front created the frontal gravity waves, a numerical simulation was performed. Rather than using a real-data simulation with a three-dimensional mesoscale model, the most simplified model and configuration suitable to the problem were selected. This approach is used to test the gravity wave hypothesis by 1) determining if the environment near the front was conducive to gravity wave ducting, 2) determining the resonant horizontal wavelength of gravity waves forced by the obstacle effect in this environment, and 3) predicting at what altitude the maximum vertical air motions would be located. The results of this simulation are then compared with the observed behavior.

The numerical model (Pihos and Wurtele 1981; Sharman et al. 1988) is two-dimensional, nonlinear, and nonhydrostatic, with cyclic lateral boundary conditions, which has recently been used to explore trapped lee wave nonstationarity (Ralph et al. 1997). The upper boundary was placed high enough (100 km) to eliminate problems with reflection from the rigid upper lid in these simulations. The horizontal domain was 200 km long, with grid spacing of 500 m horizontally and 250 m vertically. The assumption of two-dimensionality is justified based on the approximate two-dimensionality of the satellite-observed gravity waves. The relatively gradual arc occurs over a much larger scale than the horizontal wavelength. The obstacle was chosen to resemble the leading edge of the front, that is, 2.0 km high at the leading edge, dropping to 1.5 km high after 5 km horizontally. Because this shape contains contributions to the spectrum of forcing that covers a wide range of horizontal scales, its use helped ensure that the resonant mode was excited and would overwhelm nonresonant modes. Because the cyclic lateral boundary conditions precluded using an infinitely long plateau that would have better emulated the observed front, the obstacle was ramped down from 1.5 to 0.0 km over 5 km horizontally. Ground level in the model is at 1.1 km MSL, the altitude of the Amarillo, Texas, launch site. The flow is from left to right across the obstacle.

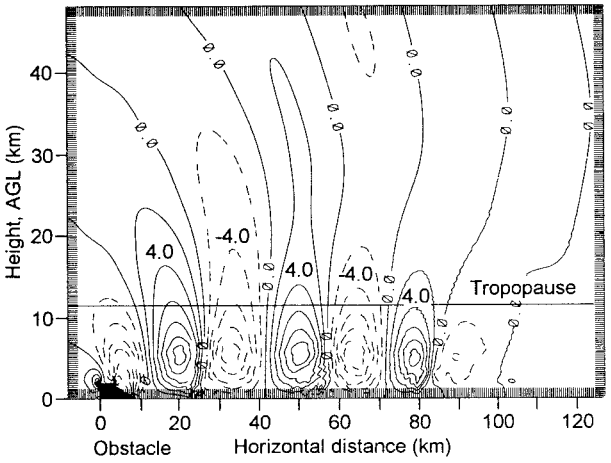

FIG. 22. Cross section of vertical motion (contoured every 2 m s^{-1}; upward, solid; downward, dashed) from 66.7 min into a nonlinear, nonhydrostatic, two-dimensional numerical simulation of lee waves formed by flow from left to right across an obstacle (solid block). The prefrontal sounding at 1200 UTC 23 February 1996 in Fig. 21b is used as the initial condition. The obstacle size and shape were chosen to emulate the observed frontal structure near its leading edge. The tropopause is marked at 11 km AGL (12 km MSL). Tick marks show grid points, which are every 250 m vertically and 500 m horizontally.

The simulation produced a train of trapped lee waves with a horizontal wavelength of 29 km, thereby confirming that the environment was conducive to wave trapping. By 66.7 min into the simulation (Fig. 22), three waves were fully developed. The waves had maximum amplitude at 5–6 km AGL (6–7 km MSL) and created vertical displacements of 2 km at this altitude (not shown).

The simulation compares well with the observations at Granada, Colorado, on 23 February 1996 (Fig. 12), where two waves were observed with maximum amplitude from 7 to 8 km MSL. The horizontal wavelength can be inferred from the time between the vertical velocity minima in Fig. 12 and the horizontal phase speed of the wave at Granada from the isochrone analysis of Fig. 9 (Table 2). On the basis of the time between vertical velocity minima of 33–45 min, and a phase speed of 8.7 m s^{-1}, the horizontal wavelength is 17–22 km. In addition, the forward slope of the updraft observed above the leading edge of the front at Granada is also evident in the simulation (note the 0 m s^{-1} contour). Another estimate of the horizontal wavelength can be made from the vertical velocity time series at Purcell, Oklahoma (Fig. 13), which contains two maxima and two minima before frontal passage that have a period of 33 min. Using the 14.0 m s^{-1} phase speed of the front at that site (Table 2) predicts a horizontal wavelength of 28 km in central Oklahoma.

The best satellite-based evidence of multiple waves shown in this paper is in the water vapor image (Fig.

15) and isochrone analysis (Fig. 16) from the 27 January 1997 case study. The satellite images from 23 February 1996 do also provide some evidence of multiple bands; however, the signal is rather weak in the published images because they do not retain the fine contrast that made them more visible in the original images seen on the computer screen. Nonetheless, quantitative brightness values measured from the screen during the event do show a signature of two bands (Figs. 7a and 8a). Figure 8a suggests a horizontal wavelength of 34 ± 5 km at 0945 UTC. Six other measurements were made directly from the original satellite images at 1215 and 1302 UTC. These revealed subtle but discernible features that are hard to see in the published versions, although the image at 0702 UTC (Fig. 6a) does still contain some hint of two bands over western Kansas, as does the image at 1402 UTC (Fig. 6c) over central Oklahoma. These measured wavelengths varied from 25 to 34 km. Four of these estimates were clustered around Amarillo and averaged 27.5 km. This area is very close in time and space to the sounding used to initialize the simulation. The other two measurements, 32 and 34 km, were over central Oklahoma.

Thus, the numerical simulation, profiler data, and satellite images all contain at least two waves with horizontal wavelengths between 17 and 34 km, mostly between 22 and 29 km. The satellite images and simulation show that the waves were roughly parallel to the front, while the simulation and profiler data also indicate that the waves had greatest vertical velocity amplitude near 6–8 km MSL, which is roughly the same layer that the water vapor images represent.

6. Summary and implications for the generation of prefrontal squall lines

Observations from the water vapor channel of the *GOES-8* satellite were combined with surface and wind profiler observations of leeside cold fronts to describe the structure and evolution of deep-tropospheric and lower-stratospheric gravity waves created by strong prefrontal, front-relative, cross-front flow (V_r) over the sharp kinematic leading edge of the fronts. Although these leeside cold fronts showed an intriguing disconnection between their thermodynamic and kinematic boundaries, the key feature for gravity wave generation appears to be the kinematic boundary, which had a head characteristic of gravity currents. The generation mechanism is analogous to mountain wave generation, but with the front acting as the obstacle. It should be noted that the obstacle effect explored here neglects the contribution to the frontal updraft resulting from front-relative postfrontal flow, but it remains clear that the gravity wave forcing is closely linked to the updraft at the leading edge of the front. The key geographical and mesoscale atmospheric conditions are summarized in Fig. 23a, while the gravity wave behavior and its relationship to the satellite-observed perturbations are shown in Figs. 23b and 23c. The mechanism by which deep-tropospheric gravity waves are created is also illustrated in Fig. 23. These waves were observed in eight cases approximately in the region outlined by Denver, Colorado; El Paso and San Antonio, Texas; and Kansas City, Missouri.

The analyses presented here indicate that the southward-propagating waves in the water vapor imagery occur within roughly 500 km east of the Rocky Mountains. Although we did not examine data from other mountainous regions, similar features have been noticed in water vapor imagery also in the lee of the Appalachian Mountains and in the lee of the Andes [R. Weldon 1998, personal communication]. The low-level blocking of a cold front east of the mountains is the key factor in setting up conditions conducive to generating observable frontal gravity waves. This can occur to either Pacific fronts or arctic fronts. In either case the blocking becomes strong enough to significantly modify the surface-frontal orientation when it encounters the part of the Rocky Mountains above 1500–2000 m MSL, which occurs north of Colorado. As a result, the front is accelerated southward, with the maximum speed occurring some 400 km east of the mountain crest, as shown schematically in Fig. 23a using the local, ground-relative, frontal propagation vector $\mathbf{c}_f$. In many cases the front becomes quasi-stationary along and parallel to the eastern side of the mountains. In contrast, the front remains in a relatively unperturbed orientation farther northeast. This creates a characteristic frontal shape highlighted in Fig. 23a by the southward bulge of the front. This shape changes with time as the surge continues.

The approximately 400-km distance east of the mountains over which there is evidence for enhanced southward progress of the front due to blocking is larger than the approximately 100-km distance expected if the very steep eastern slope of the Rockies was the only contributor to blocking the front. Recent results from Mecikalski and Tilley (1992) and Colle and Mass (1995) indicate, however, that the terrain-enhanced northerly ageostrophic postfrontal flow often extends 500 km east of the mountains, partly due to the influence of the approximately 1/500 slope of the Great Plains (Colle and Mass 1995). This distance closely matches the domain of the waves documented here.

Because the blocking and development of a surge (Colle and Mass 1995) change the frontal orientation (e.g., the mesoscale analysis of Fig. 4 shows the westward progress of the front was blocked in Colorado) the approximately geostrophic thermal wind balance that normally characterizes most frontal zones is severely disrupted. Hence the blocking changes V_r substantially because the prefrontal flow remains much less perturbed, while the frontal orientation is changed. The observations show that V_r can be very strong (>20 m s^{-1}) along the southwestern portion of the front (Fig. 23b) where its orientation is nearly normal to the prefrontal flow and the ground-relative frontal propagation

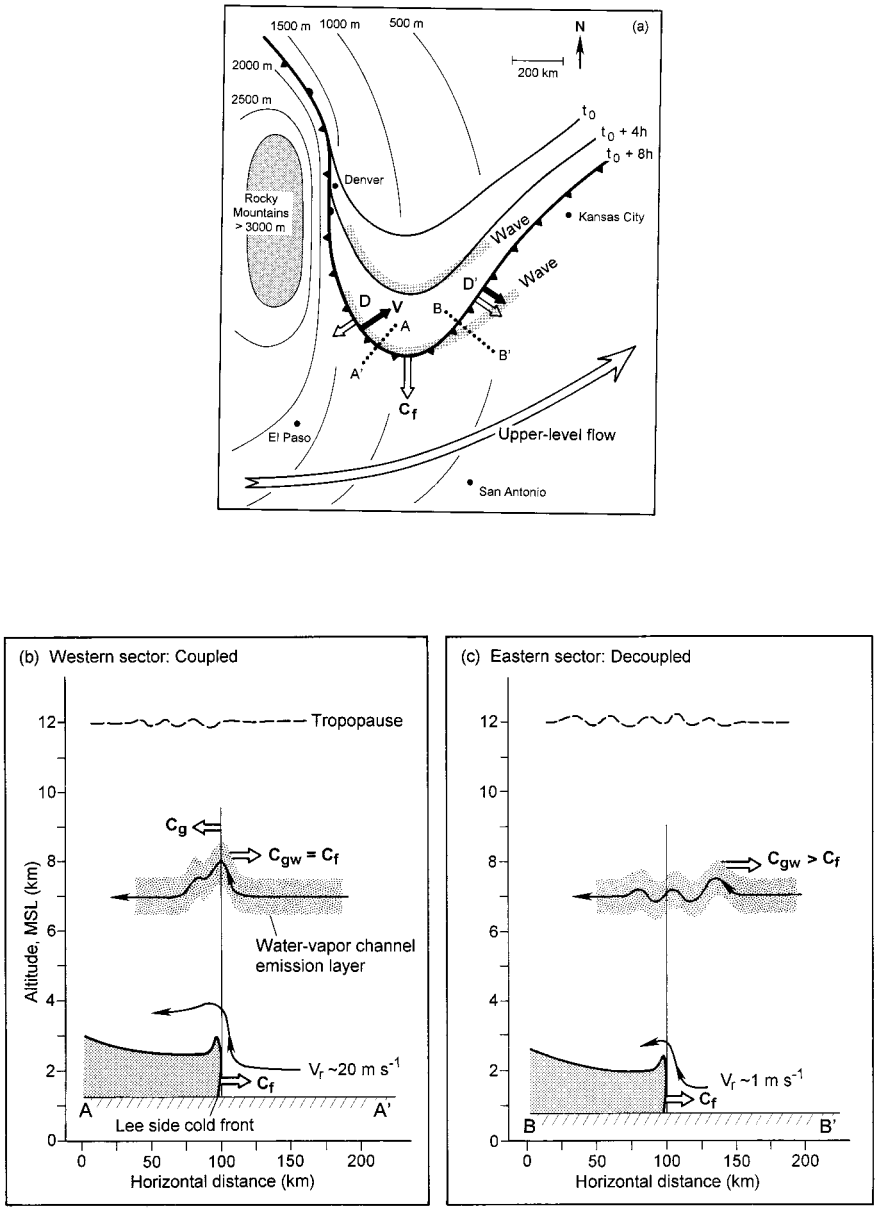

FIG. 23. Schematic summary of the structure and generation of leeside frontal gravity waves. (a) Meso-α-scale conditions that can lead to their development: a southward surge of a leeside cold front (shown at three times: t_0, t_0 + 4 h, t_0 + 8 h) is created by blocking of the surface front by the Rocky Mountains, which causes strong prefrontal, front-relative, cross-front flow ($V_r = V - c_f$) at D due to the change of frontal orientation. Local, ground-relative frontal phase velocity ($\mathbf{C}_f$; open arrow), and low-level, ground-relative, cross-front, prefrontal winds ($\mathbf{V}$; solid arrow), with vector lengths scaled to speed are shown. The upper-level flow and four cities are also marked. The observed gravity waves are shown at two times as a gray-shaded band. A smoothed representation of the terrain is also shown (altitudes, thin; regions higher than 3000 m, shaded). (b) Frontal and gravity wave structure along line A–A′ in (a); V_r, $\mathbf{C}_f$, ground-relative horizontal phase speed of the frontal gravity waves (c_{gw}), and the group velocity of the gravity waves (c_g) are shown. Vertical deflections of the midtropospheric layer typically seen by the water vapor channel are sketched (shaded), and the tropopause (dashed) is marked; (c) as in (b) but along line B–B′ in (a); (b) V_r and the frontal updraft are much stronger than in (c). (a) At D the front and gravity waves are directly coupled, whereas at D′ the waves have become decoupled from the front and have propagated ahead of the front within a wave duct.

is against the wind (at position D in Fig. 23a). In contrast, V_r is very small (<2 m s^{-1}) along the eastern portion of the front (Fig. 23c) where $\mathbf{c}_f$ nearly compensates for the cross-front flow (near D′ in Fig. 23a).

The correlation between the region along the front where V_r was strong and the region where the water vapor imagery revealed a wave supported the hypothesis that the cross-front flow was important in generating frontal gravity waves. This is also consistent with results in Snyder et al. (1993), which used idealized simulations of frontogenesis to establish that cross-front flow created the gravity waves in their simulations. It was found, however, that this correlation between the front and the waves varied along the front. While the front and the waves were approximately collocated along the western frontal segment, the waves were ahead of the front farther east, by up to 100 km.

It is proposed here that in the western region, where the front and the wave are approximately collocated, the waves are being actively generated by the front; that is, they are directly coupled. Because the regions where the waves appear ahead of the front are characterized by weak V_r, in these regions the waves and the front are decoupled. When the front enters an environment conducive to vertical trapping of gravity waves, as was shown here for the 23 February event using a numerical simulation and direct profiler observations of the wave vertical structure (e.g., Fig. 13a), the gravity waves produced by the front can be trapped and multiple wavelengths can develop. The waves can then propagate away from their source, although they will usually decay with time due to upward leakage of wave energy that results from an imperfect wave duct. Where the front is actively forcing the waves due to the obstacle effect, the wave/front geometry resembles that of mountain-induced trapped lee waves, which are normally found downstream of the obstacle. However, in regions where the front and the waves have become decoupled, the waves propagate ahead of the front where the front has slowed down and V_r has decreased. This is analogous to the nonstationary trapped lee wave behavior that Nance and Durran (1997) showed could lead to the propagation of trapped lee waves into the region upstream of the mountains that originally created them when the wave environment changed.

The study presented here has established that deep-tropospheric prefrontal gravity waves can develop in association with leeside cold-frontal surges along the eastern slope of the Rocky Mountains. These waves were documented using observations from the *GOES-8* satellite, surface instruments, and wind profilers. Profilers showed strong (± 1 m s^{-1}) vertical motions ahead of a surface front, as determined by collocated surface data and mesoscale surface-frontal analysis. These large vertical motions were observed at the same time the satellite images showed clear evidence of a wave roughly parallel to, but ahead of, the surface front. Even though ± 1 m s^{-1} prefrontal deep-tropospheric vertical motions and significant features in water vapor imagery were observed, the surface perturbations were weak: pressure amplitudes of 0.3 mb and cross-front wind perturbation amplitude of 0.5 m s^{-1}. The weakness of the perturbations at the surface most likely hid them from earlier observations, which illustrates the unique utility of the vertical profiling capabilities now available from wind profilers.

Because these gravity waves produce significant vertical motions and can occur up to at least 100 km ahead of the surface front, they could initiate deep convection in a conditionally unstable environment. Combining this knowledge with real-time satellite imagery and profiler data could provide weather forecasters in this region of severe thunderstorms a technique to help better predict the initiation of prefrontal deep convection. Although this was not the focus of the current study, it was apparent in at least one case that these waves triggered a short-lived line of deep convection over south-central Texas. When mid- or upper-tropospheric clouds are present, however, it may be more difficult to observe the waves in the water vapor imagery. It should also be noted that leeside cold fronts could produce prefrontal gravity waves that may be too weak to be observable and yet strong enough to be dynamically significant.

Acknowledgments. We appreciate several useful discussions with Dr. Chris Snyder concerning the dynamics and numerical simulations of surface cold fronts. Comments from Dr. Louisa Nance and two anonymous reviewers, as well as technical editing by Christy Sweet, improved the manuscript. Figures were expertly drafted by Jim Adams and satellite images by Al Romero.

REFERENCES

Appenzeller, C., and H. C. Davies, 1992: Structure of stratospheric intrusions into the troposphere. *Nature,* **358,** 570–572.

——, ——, and W. A. Norton, 1996: Fragmentation of stratospheric intrusions. *J. Geophys. Res.,* **101,** 1435–1456.

Barth, M. F., R. B. Chadwick, and D. W. van de Kamp, 1994: Data processing algorithms used by NOAA's wind profiler demonstration network. *Ann. Geophys.,* **12B,** 518–528.

Bluestein, H. B., 1993: *Synoptic-Dynamic Meteorology in Midlatitudes: Observations and Theory of Weather Systems.* Vol. 2. Oxford University Press, 594 pp.

Bosart, L. F., and A. Seimon, 1988: A case study of an unusually intense atmospheric gravity wave. *Mon. Wea. Rev.,* **116,** 1857–1886.

Carbone, R. E., 1982: A severe frontal rainband. Part I: Stormwide hydrodynamic structure. *J. Atmos. Sci.,* **39,** 258–279.

Clark, T. L., T. Hauf, and J. P. Kuettner, 1986: Convectively forced internal gravity waves: Results from two-dimensional numerical experiments. *Quart. J. Roy. Meteor. Soc.,* **112,** 899–925.

Colle, B. A., and C. F. Mass, 1995: The structure and evolution of cold surges east of the Rocky Mountains. *Mon. Wea. Rev.,* **123,** 2577–2610.

Crochet, M., F. Cuq, F. M. Ralph, and S. V. Venkateswaran, 1990: Clear-air radar observations of the great October storm of 1987. *Dyn. Atmos. Oceans,* **14,** 443–461.

Crook, N. A., 1988: Trapping of low-level internal gravity waves. *J. Atmos. Sci.,* **45,** 1533–1541.

Curry, M. J., and R. C. Murty, 1974: Thunderstorm-generated gravity waves. *J. Atmos. Sci.,* **31,** 1402–1408.

Doviak, R. J., S. S. Chen, and D. R. Christie, 1991: A thunderstorm-generated solitary wave observation compared with theory for nonlinear waves in a sheared atmosphere. *J. Atmos. Sci.,* **48,** 87–111.

Droegemeier, K. K., and R. B. Wilhelmson, 1987: Numerical simulation of thunderstorm outflow dynamics. Part I: Outflow sensitivity experiments and turbulence dynamics. *J. Atmos. Sci.,* **44,** 1180–1210.

Ecklund, W. L., K. S. Gage, B. B. Balsley, R. G. Strauch, and J. L., Green, 1982: Vertical wind variability observed by VHF radar in the lee of the Colorado Rockies. *Mon. Wea. Rev.,* **110,** 1451–1457.

Fovell, R. G., D. R. Durran, and J. R. Holton, 1992: Numerical simulations of convectively generated gravity waves in the stratosphere. *J. Atmos. Sci.,* **49,** 1427–1442.

Fritts, D. C., and G. D. Nastrom, 1992: Sources of mesoscale variability of gravity waves. Part II: Frontal, convective, and jet stream excitation. *J. Atmos. Sci.,* **49,** 111–127.

Gall, R. L., R. T. Williams, and T. L. Clark, 1988: Gravity waves generated during frontogenesis. *J. Atmos. Sci.,* **45,** 2204–2219.

Garner, S. T., 1989: Fully Lagrangian numerical solutions of unbalanced frontogenesis and frontal collapse. *J. Atmos. Sci.,* **46,** 717–739.

Haase, S. P., and R. K. Smith, 1989: The numerical simulation of atmospheric gravity currents. Part II: Environments with stable layers. *Geophys. Astrophys. Fluid Dyn.,* **46,** 35–51.

Hobbs, P. V., and P. O. G. Persson, 1982: The mesoscale and microscale structure and organization of clouds and precipitation in midlatitude cyclones. Part V: The substructure of narrow cold-frontal rainbands. *J. Atmos. Sci.,* **39,** 280–295.

Hutchinson, T. A., and H. B. Bluestein, 1998: Prefrontal wind shift lines in the plains of the United States. *Mon. Wea. Rev.,* **126,** 141–166.

Jin, Y., S. E. Koch, Y.-L. Lin, F. M. Ralph, and C. Chen, 1996: Numerical simulations of an observed gravity current and gravity waves in an environment characterized by complex stratification and shear. *J. Atmos. Sci.,* **53,** 3570–3588.

Klemp, J. B., R. Rotunno, and W. C. Skamarock, 1997: On the propagation of internal bores. *J. Fluid Mech.,* **331,** 81–106.

Koch, S. E., P. B. Dorian, S. Lang, G. M. Heymsfield, and F. Einaudi, 1993: A mesoscale gravity-wave event observed during CCOPE. Part IV: Stability analysis and Doppler-derived wave vertical structure. *Mon. Wea. Rev.,* **121,** 2483–2510.

Kuettner, J. P., P. A. Hildebrand, and T. L. Clark, 1987: Convection waves: Observations of gravity wave systems over convectively active boundary layers. *Quart. J. Roy. Meteor. Soc.,* **113,** 445–467.

Ley, B. E., and W. R. Peltier, 1978: Wave generation and frontal collapse. *J. Atmos. Sci.,* **35,** 3–17.

Lu, D., T. E. VanZandt, and W. L. Clark, 1984: VHF Doppler radar observations of buoyancy waves associated with thunderstorms. *J. Atmos. Sci.,* **41,** 272–282.

Mecikalski, J. R., and J. S. Tilley, 1992: Cold surges along the front range of the Rocky Mountains: Development of a classification scheme. *Meteor. Atmos. Phys.,* **48,** 249–271.

Miller, L. J., M. A. Lemone, W. Blumen, R. L. Grossman, N. Gamage, and R. J. Zamora, 1996: The low-level structure and evolution of a dry arctic front over the central United States. Part I: Mesoscale observations. *Mon. Wea. Rev.,* **124,** 1648–1675.

Mogil, H. M., 1985: The ''Blue Norther'' sudden surprising cold. *Weatherwise,* **38,** 149–150.

Mueller, C. K., and R. E. Carbone, 1987: Dynamics of a thunderstorm outflow. *J. Atmos. Sci.,* **44,** 1879–1898.

Muller, B. M., and H. E. Fuelberg, 1990: A simulation and diagnostic study of water vapor image dry bands. *Mon. Wea. Rev.,* **118,** 705–722.

Nance, L. B., and D. R. Durran, 1997: A modeling study of nonstationary trapped mountain lee waves. Part I: Mean flow variability. *J. Atmos. Sci.,* **54,** 2275–2291.

Nastrom, G., M. R. Peterson, J. L. Green, K. S. Gage, and T. E. VanZandt, 1990: Sources of gravity wave activity seen in the vertical velocities observed by the Flatland VHF radar. *J. Appl. Meteor.,* **29,** 783–792.

Neiman, P. J., and M. A. Shapiro, 1989: Retrieving horizontal temperature gradients and advections from single-station wind profiler observations. *Wea. Forecasting,* **4,** 222–233.

——, P. May, B. B. Stankov, and M. A. Shapiro, 1991: Radio acoustic sounding system observations of an Arctic front. *J. Appl. Meteor.,* **30,** 881–892.

——, ——, and M. A. Shapiro, 1992: Radio acoustic sounding system (RASS) and wind profiler observations of lower- and middle-tropospheric weather systems. *Mon. Wea. Rev.,* **120,** 2298–2313.

——, F. M. Ralph, L. Olivier, and M. J. Post, 1994: Observations of a frontal passage and associated orographically generated gravity waves along the eastern slope of the Colorado Rockies. Preprints, *Sixth Conf. on Mesoscale Processes,* Portland, OR, Amer. Meteor. Soc., 579–582.

——, ——, D. Levinson, and T. Uttal, 1995: Observations of anomalous frontal propagation and frontally forced gravity waves near steep topography. Preprints, *Seventh Conf. on Mountain Meteorology,* Breckenridge, CO, Amer. Meteor. Soc., 149–155.

——, F. M. Ralph, M. A. Shapiro, B. F. Smull, and D. Johnson, 1998: An observational study of fronts and frontal mergers during the phasing of Arctic and Pacific-polar synoptic-scale waves over the continental United States. *Mon. Wea. Rev.,* **126,** 2521–2554.

Parsons, D. B., M. A. Shapiro, R. M. Hardesty, R. J. Zamora, and J. M. Intrieri, 1991: The finescale structure of a west Texas dryline. *Mon. Wea. Rev.,* **119,** 1242–1258.

Pihos, G. G., and M. G. Wurtele, 1981: An efficient code for the simulation of non-hydrostatic flow over obstacles. NASA CR 3385, 137 pp. [NTIS N81-23762.]

Prichard, I. T., L. Thomas, and R. M. Worthington, 1995: The characteristics of mountain waves observed by radar near the west coast of Wales. *Ann. Geophys.,* **13,** 757–767.

Ralph, F. M., 1996: Observations of 250-km-wavelength clear-air eddies and 750-km-wavelength mesocyclones associated with a synoptic-scale midlatitude cyclone. *Mon. Wea. Rev.,* **124,** 1199–1210.

——, M. Crochet, and S. V. Venkateswaran, 1992: A study of mountain lee waves using clear-air Doppler radar. *Quart. J. Roy. Meteor. Soc.,* **118,** 597–627.

——, ——, and ——, 1993a: Observations of a mesoscale ducted gravity wave. *J. Atmos. Sci.,* **50,** 3277–3291.

——, C. Mazaudier, M. Crochet, and S. V. Venkateswaran, 1993b: Doppler sodar and radar wind profiler observations of gravity wave activity associated with a gravity current. *Mon. Wea. Rev.,* **121,** 444–463.

——, P. J. Neiman, D. W. van de Kamp, and D. C. Law, 1995: Using spectral moment data from NOAA's 404-MHz radar wind profilers to observe precipitation. *Bull. Amer. Meteor. Soc.,* **76,** 1717–1739.

——, ——, T. L. Keller, D. Levinson, and L. Fedor, 1997: Observations, simulations, and analysis of nonstationary trapped lee waves. *J. Atmos. Sci.,* **54,** 1308–1333.

Sato, K., 1990: Vertical wind disturbances in the troposphere and lower stratosphere observed by the MU radar. *J. Atmos. Sci.,* **47,** 2803–2817.

Schultz, D. M., W. E. Bracken, L. F. Bosart, G. J. Hakim, M. A. Bedrick, M. J. Dickenson, and K. R. Tyle, 1997: The 1993 Superstorm cold surge: Frontal structure, gap flow, and tropical impact. *Mon. Wea. Rev.,* **125,** 5–39.

——, ——, and ——, 1998: Planetary- and synoptic-scale signatures associated with Central American cold surges. *Mon. Wea. Rev.,* **126,** 5–27.

Scorer, R. S., 1949: Theory of lee waves of mountains. *Quart. J. Roy. Meteor. Soc.,* **75,** 41–56.

Seitter, K. L., and H. S. Muench, 1985: Observation of a cold front with rope cloud. *Mon. Wea. Rev.,* **113,** 840–848.

Shapiro, M. A., 1984: Meteorological tower measurements of a surface cold front. *Mon. Wea. Rev.,* **112,** 1634–1639.

——, T. Hampell, D. Rotzoll, and F. Mosher, 1985: The frontal hydraulic head: A micro-α-scale (1 km) triggering mechanism for mesoconvective weather sytems. *Mon. Wea. Rev.,* **113,** 1166–1183.

Sharman, R. D., T. L. Keller, and M. G. Wurtele, 1988: Incompressible and anelastic flow simulations on numerically generated grids. *Mon. Wea. Rev.,* **116,** 1124–1136.

Simpson, J. E., 1987: *Gravity Currents in the Environment and the Laboratory.* John Wiley and Sons, 244 pp.

Smith, R. B., 1979: The influence of mountains on the atmosphere. *Advances in Geophysics,* Vol. 21, Academic Press, 87–230.

Snyder, C., W. C. Skamarock, and R. Rotunno, 1993: Frontal dynamics near and following frontal collapse. *J. Atmos. Sci.,* **50,** 3194–3211.

Stobie, J. G., L. W. Uccellini, and F. Einaudi, 1983: A case study of gravity waves–convective storms interaction: 9 May 1979. *J. Atmos. Sci.,* **40,** 2804–2830.

Tepper, M., 1950: A proposed mechanism of squall lines: The pressure jump line. *J. Meteor.,* **7,** 21–29.

Trexler, C. M., 1997: Vertical structure of a mesoscale gravity wave event observed during STORMFEST: A comparative analysis between in situ and remote sensing observations, numerical simulation, and a linear theory predictions. M.S. thesis, Department of Marine, Earth, and Atmospheric Sciences, North Carolina State University at Raleigh, 223 pp.

Uccellini, L. W., and S. E. Koch, 1987: The synoptic setting and possible energy sources for mesoscale wave disturbances. *Mon. Wea. Rev.,* **115,** 721–729.

Wang, P.-Y., J. E. Martin, J. D. Locatelli, and P. V. Hobbs, 1995: Structure and evolution of winter cyclones in the central United States and their effects on the distribution of precipitation. Part II: Arctic fronts. *Mon. Wea. Rev.,* **123,** 1328–1344.

Weckwerth, T. M., and R. M. Wakimoto, 1992: The initiation and organization of convective cells atop a cold-air outflow boundary. *Mon. Wea. Rev.,* **120,** 2169–2187.

Weldon, R. B., and S. J. Holmes, 1991: Water vapor imagery: Interpretations and applications to weather analysis and forecasting. NOAA Tech. Rep. NESDIS 57, 213 pp. [Available from NTIS, Springfield, VA 22161; NTIS N 92–14565/5.]

Worthington, R. M., and L. Thomas, 1996: Radar measurements of critical-layer absorption in mountain waves. *Quart. J. Roy. Meteor. Soc.,* **122,** 1263–1282.

Young, G. S., and R. H. Johnson, 1984: Meso- and microscale features of a Colorado cold front. *J. Climate Appl. Meteor.,* **23,** 1315–1325.